BIOENGINEERING

Electromechanical cardioplasty using a wrapped elasto-conductive epicardial mesh

Jinkyung Park,[1,2]* Suji Choi,[1,3]* Ajit H. Janardhan,[4] Se-Yeon Lee,[5,6] Samarth Raut,[7] Joao Soares,[7] Kwangsoo Shin,[1,3] Shixuan Yang,[8] Chungkeun Lee,[9] Ki-Woon Kang,[10] Hye Rim Cho,[1,11] Seok Joo Kim,[1,3] Pilseon Seo,[1,3] Wonji Hyun,[1,3] Sungmook Jung,[1,3] Hye-Jeong Lee,[12] Nohyun Lee,[13] Seung Hong Choi,[1,11] Michael Sacks,[7] Nanshu Lu,[8,14] Mark E. Josephson,[15] Taeghwan Hyeon,[1,2,3†] Dae-Hyeong Kim,[1,3†] Hye Jin Hwang[5,15†‡]

Heart failure remains a major public health concern with a 5-year mortality rate higher than that of most cancers. Myocardial disease in heart failure is frequently accompanied by impairment of the specialized electrical conduction system and myocardium. We introduce an epicardial mesh made of electrically conductive and mechanically elastic material, to resemble the innate cardiac tissue and confer cardiac conduction system function, to enable electromechanical cardioplasty. Our epicardium-like substrate mechanically integrated with the heart and acted as a structural element of cardiac chambers. The epicardial device was designed with elastic properties nearly identical to the epicardial tissue itself and was able to detect electrical signals reliably on the moving rat heart without impeding diastolic function 8 weeks after induced myocardial infarction. Synchronized electrical stimulation over the ventricles by the epicardial mesh with the high conductivity of 11,210 S/cm shortened total ventricular activation time, reduced inherent wall stress, and improved several measures of systolic function including increases of 51% in fractional shortening, ~90% in radial strain, and 42% in contractility. The epicardial mesh was also capable of delivering an electrical shock to terminate a ventricular tachyarrhythmia in rodents. Electromechanical cardioplasty using an epicardial mesh is a new pathway toward reconstruction of the cardiac tissue and its specialized functions.

INTRODUCTION

The heart efficiently pumps blood by coordinated contractions made by the rapid conduction of electrical impulses. Heart failure is often accompanied by impairment of, or injury to, the specialized His-Purkinje conduction system (*1*). Currently, patients undergo medical therapy in an attempt to reverse adverse mechanical remodeling. Biventricular pacing attempts to improve electrical dyssynchrony but can only be applied to a subset of patients and has a significant non-responder rate associated with it. Thus, a comprehensive approach that partially compensates for impaired myocardium and substitutes for functions of the diseased electrical conduction system would be a promising treatment for heart failure patients.

Biventricular pacing, for which a subset of heart failure patients may qualify, has been proven to rapidly enhance cardiac function, alleviate symptoms, and improve long-term survival in numerous clinical trials (*2*). This type of pacing improves inefficient pumping activity by reducing the discoordination of contractions in diseased hearts by simultaneously pacing both chambers. Therefore, it has been proposed as a standard therapy by the American College of Cardiology and the American Heart Association in the subset of patients who may benefit (*3*). Despite these positive attributes, biventricular pacing involves the activation of the myocardium through electrical current sources originating from only two point electrodes located in the dilated ventricle, rather than a more comprehensive approach where large areas of the myocardium are activated simultaneously.

The concept of cardiomyoplasty, augmenting the function of diseased myocardium through a biventricular wrap, was introduced in the 1980s and involved wrapping the skeletal muscle (latissimus dorsi) around the heart to prevent postmyocardial infarction (post-MI) remodeling and to augment systolic function by pacing skeletal muscle flap (*4*). Unfortunately, this initially attractive therapy faded from clinical practice because hemodynamic improvement in systolic function was not consistently demonstrated, and sudden death and arrhythmic events occurred during follow-up. Instead, a device encircling the heart was hypothesized to act as a structural subcomponent of myocardium to share myofiber stress as well as reduce the size of cardiac chambers

[1]Center for Nanoparticle Research, Institute for Basic Science, Seoul 08826, Republic of Korea. [2]Graduate School of Convergence Science and Technology, Seoul National University, Suwon, Gyeonggi-do 16229, Republic of Korea. [3]School of Chemical and Biological Engineering, Institute of Chemical Processes, Seoul National University, Seoul 08826, Republic of Korea. [4]Division of Cardiac Electrophysiology, Health First Medical Group, Cocoa Beach, FL 32931, USA. [5]Yonsei Cardiovascular Research Center and Cardiovascular Research Institute, Severance Hospital, Yonsei University Health System, Seoul 03722, Republic of Korea. [6]Institute for Biomedical Convergence, College of Medicine, Catholic Kwandong University, Gangneung-si, Gangwon-do 25601, Republic of Korea. [7]Center for Cardiovascular Simulation, Institute for Computational Engineering and Sciences, University of Texas at Austin, Austin, TX 78712, USA. [8]Center for Mechanics of Solids, Structures and Materials, Department of Aerospace Engineering and Engineering Mechanics, Texas Materials Institute, University of Texas at Austin, Austin, TX 78712, USA. [9]School of Electrical and Electronic Engineering, Yonsei University, Seoul 03722, Republic of Korea. [10]Division of Cardiology, Eulji University Hospital, Eulji University College of Medicine, Daejeon 35233, Republic of Korea. [11]Department of Radiology, Seoul National University College of Medicine, Seoul 03080, Republic of Korea. [12]Department of Radiology, Research Institute of Radiological Science, Severance Hospital, Yonsei University Health System, Seoul 03722, Republic of Korea. [13]School of Advanced Materials Engineering, Kookmin University, Seoul 02707, Republic of Korea. [14]State Key Laboratory of Digital Manufacturing Equipment and Technology, Huazhong University of Science and Technology, Wuhan 430074, China. [15]Harvard-Thorndike Electrophysiology Institute, Cardiovascular Division, Department of Medicine, Beth Israel Deaconess Medical Center, Harvard Medical School, Boston, MA 02215, USA.
*These authors contributed equally to this work.
†Corresponding author. Email: hhwang@bidmc.harvard.edu (H.J.H.); dkim98@snu.ac.kr (D.-H.K.); thyeon@snu.ac.kr (T.H.)
‡Present address: Cardiovascular Division, Department of Medicine, Beth Israel Deaconess Medical Center, Harvard Medical School, Boston, MA 02215, USA.

thereby contributing to a positive remodeling process and subsequent improvement of pumping activity (*5*–*7*). Human trials using devices wrapping the heart, such as the electrically nonconductive polyester mesh wrap CorCap (Acorn Cardiovascular Inc.) and the nitinol mesh wrap HeartNet (Paracor Medical Inc.), also showed controversial results. In a randomized clinical trial, HeartNet wrapping the heart in patients with heart failure had no effect on functional end points, particularly peak oxygen consumption or survival (*5*). The CorCap trial did demonstrate significant improvement in the prevention of ventricular remodeling, but there were controversial results in long-term survival (*6*, *7*).

Here, we introduce electromechanical cardioplasty using an epicardial mesh designed to both mechanically integrate with the heart and act as a structural element of cardiac chambers, enabling global pacing to stimulate the whole ventricle. We also instilled the electrical function of a cardiac conduction system (His bundles and Purkinje fiber network) into the mesh to deliver impulses to the whole ventricular myocardium in concert, rather than merely to small point electrodes in the ventricles. To achieve these, we explored candidate materials to be elastic and conductive as in cardiac tissue. Recently developed conductive and stretchable materials, such as gold-based composites (*8*, *9*) and carbon nanotube–based composites (*10*, *11*), have shown potential as elasto-conductive materials. However, many technical issues, including low conductivity, poor elasticity, and/or high resistance change induced by strains, still remain. Meanwhile, silver nanowire (AgNW) networks are known to maintain high conductivity under repeatedly applied strains due to their mechanical deformability and highly percolated structures (*12*, *13*). Styrene-butadiene-styrene (SBS) rubber, a biocompatible thermoplastic polymer, has high elasticity and reshaping capability because of its physically cross-linked structure (*14*, *15*). We chose AgNW and SBS rubber to fabricate the mesh-shaped substrate resembling elastic and electrical properties of cardiac tissue.

In postinfarct rats, the epicardial mesh integrated with the heart preserved diastolic relaxation, reduced inherent wall stress by sharing cardiac load as a structural component, improved cardiac contractile function through synchronized electrical stimulation, and terminated ventricular tachyarrhythmia as an epicardial defibrillator. Our study demonstrates an improved therapeutic approach to electromechanical cardioplasty using an epicardial device that reconstructs the cardiac tissue form and its specialized functions.

RESULTS

The epicardial mesh is soft, elastic, and highly conductive

The cardiac conduction system spreads across the endocardial surface of the ventricles and rapidly transmits electrical signals from endocardium to epicardium by interfacing directly with cardiac muscles to enable coordinated contractions of the heart. For the elasto-conductive mesh device design, we attempted to imitate the basic structure and function of the heart (Fig. 1A). To confer elasticity and stable electrical conductivity, we fabricated a homogeneous nanocomposite of AgNW and SBS rubber. Ligand exchange of AgNW (LE-AgNW) is necessary for homogeneous dispersion in the organic-phase SBS solution (*15*–*17*). Polyvinylpyrrolidone (PVP) ligand of AgNW was partially exchanged to hexylamine (HAm) using $NOBF_4$ (Fig. 1B), allowing for a phase transfer of the water-dispersed AgNW to the organic phase. The increased peak intensity of N–H bond stretching in the Fourier transform infrared spectroscopy spectra confirmed successful ligand exchange reaction (fig. S1A). Compared to AgNW/SBS nanocomposite without ligand exchange, LE-AgNW/SBS nanocomposite exhibited consistently lower impedance for different frequency inputs (Fig. 1C) and larger charge injection for different voltage inputs (Fig. 1D), indicating stable electrical conduction of the LE-AgNW/SBS nanocomposite. The conductivity of LE-AgNW/SBS nanocomposite also depended on the mixing ratio of LE-AgNW to SBS (fig. S1B). As the proportion of LE-AgNW increased, electrical conductivity improved, but mechanical elasticity was deteriorated (fig. S1C), demonstrating that the optimal ratio of LE-AgNW and SBS is required to achieve both good electrical conductivity and elasticity. A nanocomposite with LE-AgNW/SBS ratio of 65:35 conferred the optimal conductivity of 11,210 S/cm, which is 1000-fold higher than conventional commercial conductive rubber (<10 S/cm).

Next, we optimized the elastic properties of the LE-AgNW/SBS nanocomposite. Encircling the heart with a stiff film may decrease diastolic compliance, thereby aggravating heart failure symptoms, as shown in cardiac diseases such as constrictive pericarditis or restrictive cardiomyopathy (*18*). Therefore, we aimed to create a device with mechanical properties similar to that of the rat myocardium to conform anatomically to and integrate with the epicardial surface. To tailor mechanical elasticity of the LE-AgNW/SBS nanocomposite, a mesh design was applied using a polydimethylsiloxane (PDMS) mold (Fig. 1E and fig. S2). To improve durability, the LE-AgNW/SBS nanocomposite was covered by an SBS layer. The elastic modulus was 44.71 ± 7.54 kPa in serpentine mesh and 3.39 ± 0.849 kPa in hyperserpentine mesh, depending on the extent of curvature of the serpentine structure. The serpentine and hyperserpentine meshes exhibited remarkably softer mechanical properties than the film of the same material (Fig. 1F).

We then resected epicardial tissue sheets from rat hearts and measured the elastic modulus of 2-mm-thick epicardial tissue sheets, which was 34.67 ± 6.2 kPa (n = 3). The circumferential strain (change of circumference between end diastole and end systole divided by circumference at end diastole) in the outer layer of the heart estimated by echocardiography was 14.1 ± 1.4% in control hearts (n = 4) and 4.6 ± 0.5% in 8-week post-MI rat hearts (n = 3) (Fig. 1G). On the basis of these results, we chose a serpentine mesh design with elasticity nearly identical to that of epicardium within a physiological strain range of 20% in cardiac movement. Under these applied strains, the epicardial mesh exhibited minimal change in its electrical resistance (Fig. 1H). The electrical property was consistent with only 1.02-fold increase over 10,000 repetitive stretching cycles, approximating 3 hours of cardiac movement in humans (Fig. 1H, inset).

Personalized design is made using a 3D printed heart

The epicardial mesh was designed as shown in Fig. 2A. The size of the electrodes was large enough to cover the entire ventricles [right ventricle (RV), 12.5 × 10 mm; left ventricle (LV), 17 × 10 mm; thickness, 100 μm]. This design enabled the current flow by electrical stimulation to be broadly distributed, allowing rapid propagation of depolarization of the myocardium as shown in the previous reports (*19*, *20*). The device was composed of two wide serpentine mesh electrodes, which were positioned on the RV and the LV, with an insulating part between the cathode and anode (denoted as I) and supporting parts at the ends (denoted as S) to assist wrapping of the device around the heart (Fig. 2A). The mass of silver was about 20 mg per device.

The outer part of the epicardial mesh was coated with an SBS to insulate the electrodes (Fig. 2A, right). The elasticity of the device was

confirmed by pulling (L_0 = 60 mm to L_1 = 90 mm) and releasing the mesh (L_1 to L_0'= 60 mm) (Fig. 2B and movie S1). Using a 3D image created by cardiac computed tomography (CT) (Fig. 2C), we could make an anatomically personalized design for the rodents. The final design was confirmed by wrapping a 3D printed heart model with the mesh tailored to the rat's cardiac parameters, including the size of each part (RV, LV, I, and S) and the overall size measured at systole (Fig. 2D).

Computer simulations estimate the mechanical effect of the epicardial mesh

We estimated the mechanical effects of the epicardial mesh on rat heart diastolic function through a biventricular finite element model constructed from high-resolution CT images, with continuous transmural fiber orientations across its thickness (Fig. 3A). Diastolic expansions of three cases on the wrapping model (Fig. 3B) were compared: (i) without any wrap on the heart, (ii) with the wrap using epicardial mesh

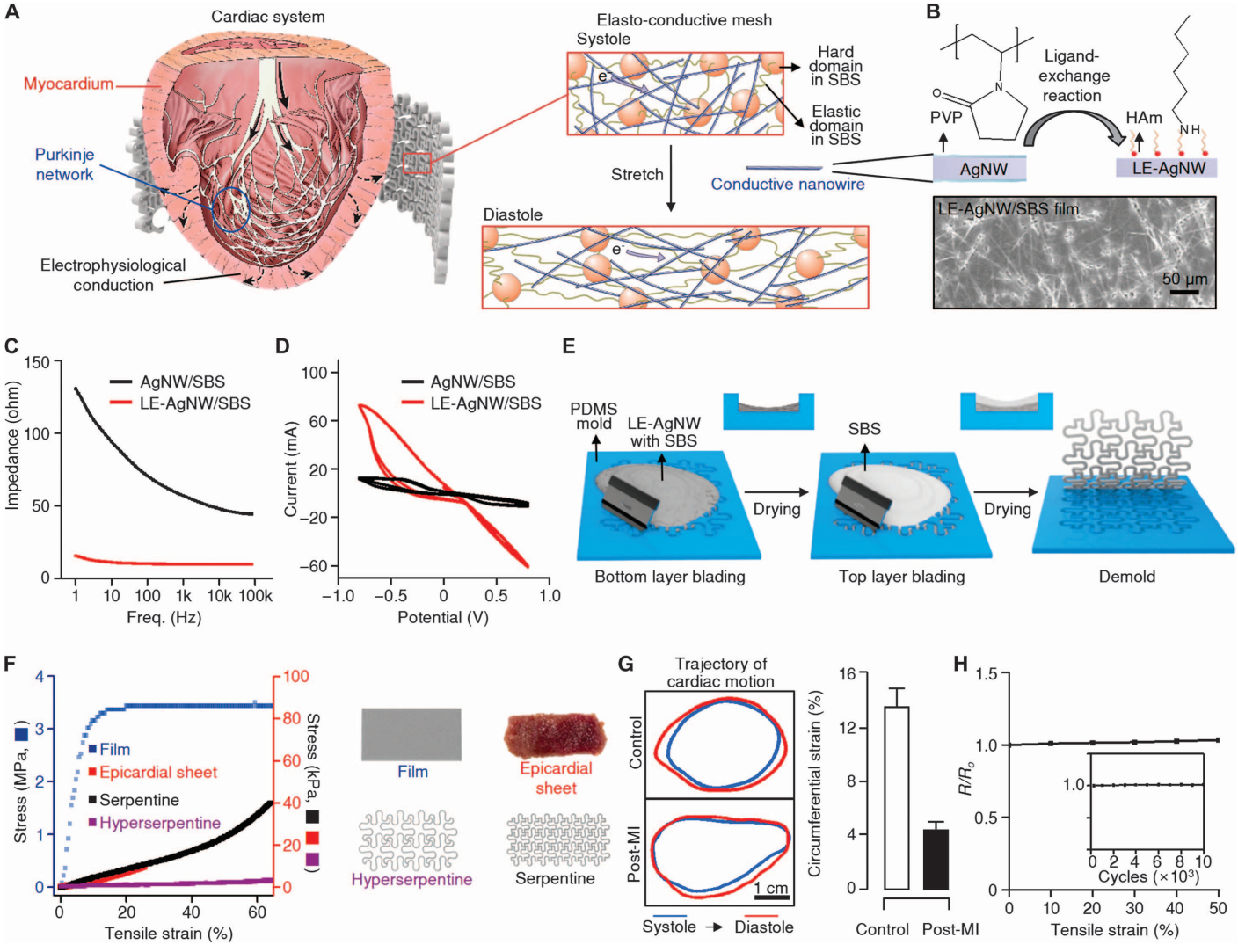

Fig. 1. Materials and design strategy of an elasto-conductive epicardial mesh. (**A**) Schematic illustration of the design strategy of an epicardial mesh for electromechanical cardioplasty in accordance with electrophysiological conduction in the cardiac system. Conductive nanowires were homogeneously dispersed in SBS rubber, allowing for electrical signal (e^-) transfer during the entire cardiac cycle. (**B**) Scheme of the reaction for LE-AgNW (top). The ligand of AgNW was exchanged from PVP to HAm via $NOBF_4$ treatment. A scanning electron microscopy image of LE-AgNW/SBS nanocomposite is shown. (**C**) Representative impedance measurement of the initial and ligand-exchanged films as a function of frequency (Freq.) of alternating current. (**D**) Representative cyclic voltammetry analysis. Current was measured during a potential sweep from −0.8 to 0.8 V. (**E**) Schematic illustration of the epicardial mesh fabrication. (**F**) Average stress-strain curves of epicardial sheet, serpentine mesh (epicardial mesh), hyperserpentine mesh, and film. (**G**) Trajectory of movements of the outer layer of control and post-MI rat heart at end systole (blue) and end diastole (red) measured by two-dimensional (2D) echocardiography. Circumferential strain of the outer layer of the heart was calculated in control hearts (n = 4) and 8-week post-MI hearts (n = 3). (**H**) Representative relative resistance changes of the epicardial mesh at increasing tensile strains. Cyclic test of the epicardial mesh when applying 15% tensile strain (inset).

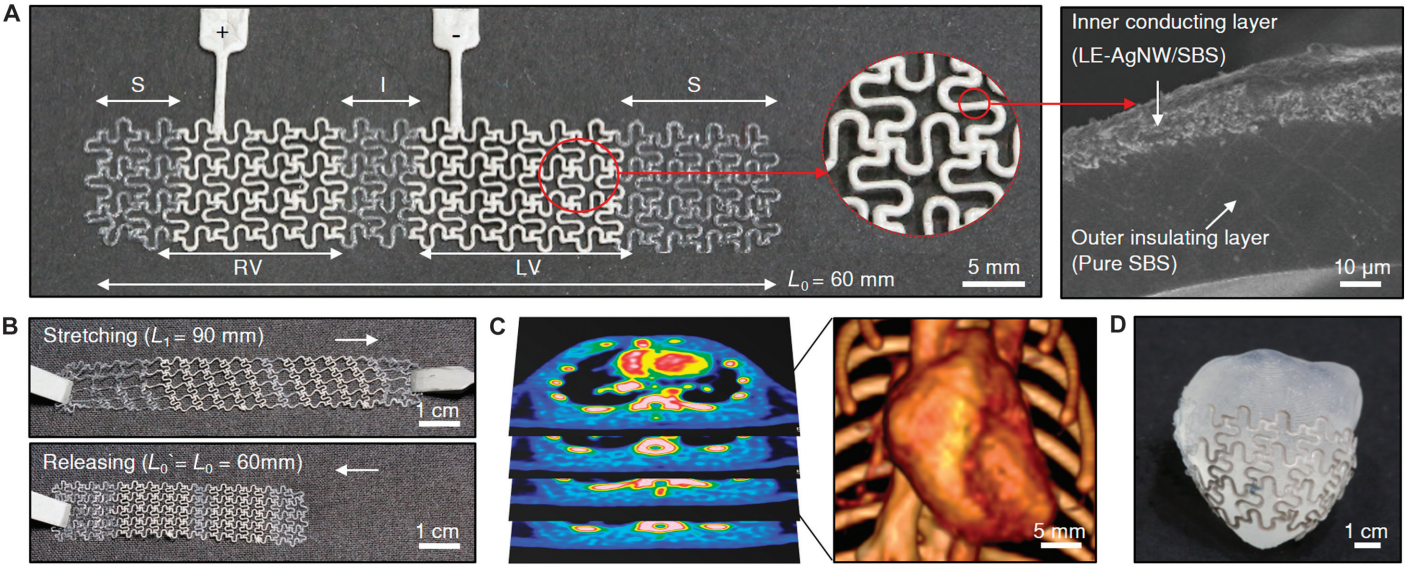

Fig. 2. Personalized design of the epicardial mesh. (**A**) Panoramic, 2D view of the epicardial mesh composed of an insulated part (I) connecting RV electrode (+), LV electrode (–), and structural supporting parts (S). A scanning electron microscopy image on the right shows the cross section of the mesh electrode to illustrate the conducting (inner) and insulating (outer) layers. The total thickness of the mesh electrode is 100 μm. (**B**) Manual testing of the elasticity of the epicardial mesh [initial length (L_0) = 60 mm, stretched length (L_1) = 90 mm, and released length (L_0') = 60 mm)]. (**C**) Stacked CT images of a rat heart (left) and its 3D heart reconstruction image derived from the 2D layers (right). (**D**) A photograph of the epicardial mesh encircling the 3D printed heart model from (C).

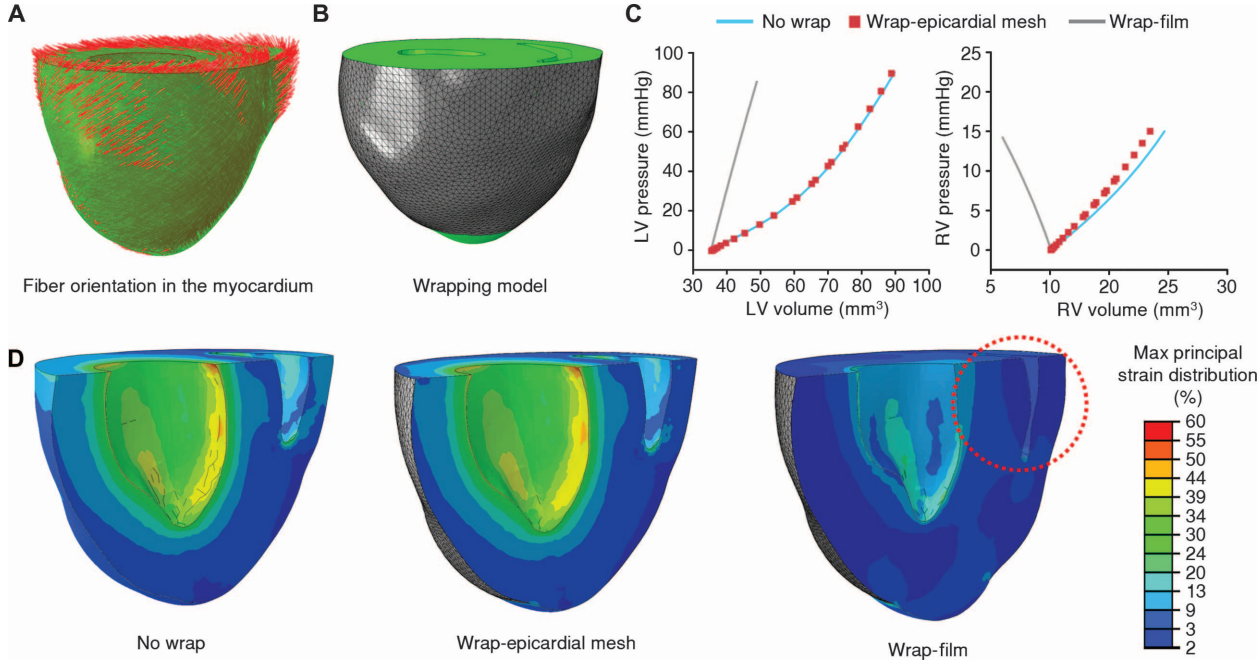

Fig. 3. Theoretical estimation of the mechanical influences of devices on the heart by the computer simulation. (**A**) Biventricular finite element model of a representative rat heart with the fiber orientations of the anisotropic myocardium. (**B**) Finite element model of the rat heart, wrapped by the gray shell elements representing the epicardial wrapping (mesh or film). (**C**) Effects of the mesh and the film on the end-diastolic pressure-volume relationship of LV and RV. Each red point indicates pressure-volume value in a simulated heart wrapped by the epicardial mesh. (**D**) Maximum principal strain distribution without any wrap (left), with the epicardial mesh wrap (middle), and with the film wrap (right). Encircled area indicates RV collapse.

(E = 50 kPa), and (iii) with the wrap of unpatterned device (continuous thin film; E = 47 MPa). The effects of the epicardial mesh or film wrap on end-diastolic pressure-volume relationship were analyzed (Fig. 3C). Compared to the control (no wrapping), the film wrap constrained heart inflation and elevated end-diastolic pressure, possibly leading to increased backward pressure to the left atrium and pulmonary vascular congestion. In contrast, the epicardial mesh wrap did not show any appreciable effect. Notably, the film of the LE-AgNW/SBS nanocomposite caused diastolic collapse in the RV in silico (Fig. 3D), implying a significant risk of hemodynamic instability. In contrast, the epicardial mesh wrap did not affect the shape or curvature of ventricular chambers during the simulated cardiac cycle.

The epicardial mesh integrates with the moving rat heart without impeding diastolic relaxation

We tested whether the epicardial mesh maintained conformal contacts on the moving heart in vivo and consistently monitored intrinsic myocardial electrical activities. A custom-designed epicardial mesh covering the entire surface of both ventricles was implanted in a control rat (Fig. 4A). Baseline surface electrocardiogram (ECG), conventional bipolar electrode, and epicardial mesh simultaneously detected cardiac electrical activity (Fig. 4B). Phase consistency of the whole electrograms and the severity of the baseline drift were compared between a conventional bipolar electrode and an epicardial mesh. Electrograms recorded from the epicardial mesh exhibited stable signals without any visible baseline drifts, whereas baseline drift was evident in electrograms from the conventional bipolar electrode with a 2-mm interval placed on the RV surface (Fig. 4, B and C). After subtracting QRS-T complexes, average absolute deviation of the baseline drift was significantly less with the epicardial mesh than with the conventional electrode (Fig. 4D), suggesting that the epicardial mesh was well integrated to the epicardial surface of the moving heart.

Next, we tested the influence of the epicardial mesh with elastic properties on diastolic relaxation and myocardial stress. One desirable effect was to reduce stress of the host myocardium by sharing it with the introduced device without disturbing diastolic relaxation. MI is the most common cause of human heart failure, and thereby, we induced an MI in 36 rats (19 survived by 8 weeks after MI) in this test. Areas of scar in the post-MI model created by left anterior descending artery (LAD) ligation were confirmed histologically using Masson's trichrome stain or by gross specimen examination in all survived rats.

The effect of the epicardial mesh on diastolic function was evaluated at baseline and during right atrial pacing and mesh pacing at the same cycle length of 420, 300, and 280 ms in control (n = 5) and 8-week post-MI rats (n = 5), because diastolic relaxation is influenced by heart rate. The implanted epicardial mesh did not significantly change the LV end-diastolic pressure (LVEDP), an index of compliance, or τ, an index of diastolic relaxation at baseline (sinus rhythm) and during electrical stimulation in the control and post-MI rats (all $P > 0.05$ by linear mixed model; Fig. 5A). Furthermore, we did not observe a constrictive pattern of LV pressure in all experimental rat hearts (Fig. 5B).

Mechanical stress on the myocardium exerts tension on cardiomyocytes, stimulating various pathophysiologic responses (*21*). We sought to investigate the impact of the epicardial mesh as a structural component

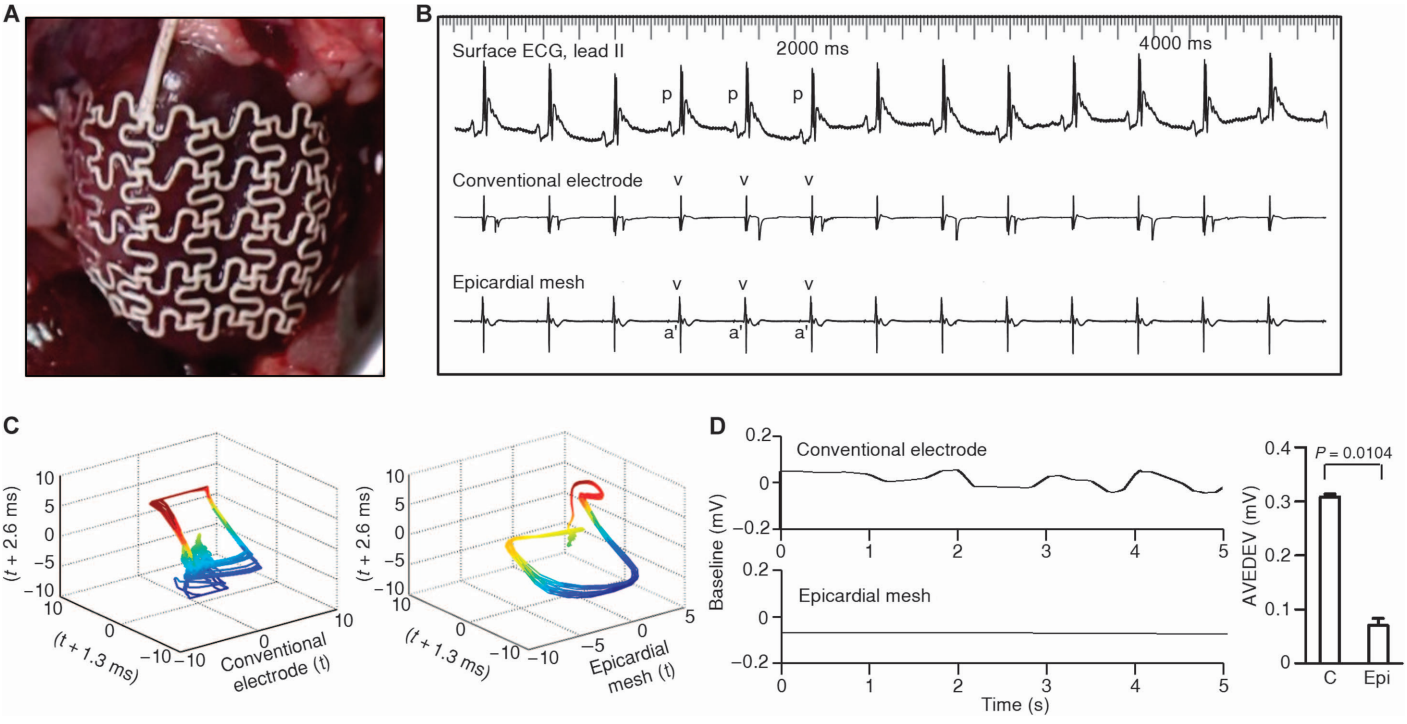

Fig. 4. Coupling of the epicardial mesh to the rat heart. (**A**) Photograph of the epicardial mesh implanted in a control heart. (**B**) Surface ECG (lead II) and intracardiac electrograms recorded from a conventional electrode on the RV and the epicardial mesh encircling the heart. p, p-wave; v, ventricle; a', atrium. (**C**) 3D phase attractor of phase consistency of electrograms in (B) recorded from a conventional electrode and the epicardial mesh. (**D**) From intracardiac electrograms of the conventional electrode (C) and epicardial mesh (Epi), the baselines are extracted using peak analysis software. Average absolute deviation (AVEDEV) was calculated from the baseline. Data are averages ± SEM (n = 3). P value was determined by unpaired Student's t test.

on myocardial stress. To measure changes in wall stress, we recorded LV pressure with a Millar catheter and simultaneously measured mid-LV radial strain by echocardiography. During the electrical stimulation with the epicardial mesh, longitudinal wall stress was reduced during the entire cardiac cycle (diastole and systole) in the post-MI heart and slightly reduced in the control (Fig. 5C). In post-MI hearts, the epicardial mesh reduced the peak longitudinal wall stress of 654.6 kdyne/cm^2 at baseline to 569.1 kdyne/cm^2. During the overall time of systole, the average of wall stress reduction by the epicardial mesh was 46.9 kdyne/cm^2. During the overall time of diastole, wall stress was 12.0 kdyne/cm^2.

Electrical stimulation restores total ventricular activation time and improves systolic function

We investigated whether electrical stimulation by the epicardial mesh could substitute the basic function of His-Purkinje fibers by shortening total activation time of the ventricles (QRS duration) and activating heart muscles synchronously. The mean QRS duration at baseline in 8-week post-MI rats was significantly more prolonged than in controls (fig. S3A), reflecting damages to myocardium and/or the conduction system due to underlying disease. Whole-ventricle pacing at a cycle length of 280 ms was then continuously delivered through the epicardial mesh in control and post-MI rats (fig. S3B). In controls, the duration of the QRS complex during epicardial mesh pacing (26.5 ± 0.7 ms) was nearly identical to that at baseline (28.6 ± 0.7 ms) (Fig. 6, A and B, and fig. S3A). The total activation time by the epicardial mesh pacing approximates the healthy His-Purkinje conduction system. Epicardial mesh pacing in post-MI hearts resulted in a QRS duration similar to that observed in control hearts during sinus rhythm or epicardial mesh pacing, reducing the QRS duration from 38.9 ± 3.6 ms at baseline to a normal range of 26.1 ± 3.0 ms (fig. S3A). Figure 4B also demonstrates reduction of QRS duration by mesh pacing in all post-MI rats.

All post-MI rats that completed the electrophysiology study showed the effective normalization of QRS duration (≤27 ms) by epicardial mesh pacing, except for one animal where QRS duration was reduced from 66 to 37 ms. To evaluate the possibility that QRS duration varied with heart rate, we measured the QRS duration at multiple heart rates in all rats. We found that heart rates were unrelated to QRS duration (fig. S4A). We also found that epicardial mesh pacing at 90% of the baseline cycle length (10% faster than the native heart rate) shortened the QRS duration compared to the nonpaced, native QRS duration at baseline (fig. S4B), but this was tested only in two of the animals from Fig. 6B (that had the cycle lengths of mesh pacing similar to that of baseline) and would need further exploration. These data suggest that electrical stimulation therapy with the epicardial mesh in an 8-week post-MI heart restores overall electrical activation time of the ventricles to near-normal activation time.

To assess mechanical synchrony of the myocardium, radial strains were observed at all six mid-LV segments in control and post-MI hearts using speckle tracking imaging (fig. S5, A and B). Examples of speckle tracking of strain are shown in fig. S5A for baseline (sinus rhythm) and RV pacing (a positive control showing dyssynchrony, only for visual demonstration of the method here) and mesh pacing (synchrony). These images were quantified at various points (color coded in fig. S5A) and revealed that dyssynchronous systolic contractions were present in the post-MI rats (fig. S5B). However, electrical stimulation through the epicardial mesh restored synchronous activation of all segments, which agrees with the shortening of the total electrical activation time of ventricles.

We further assessed whether electrical stimulation by the epicardial mesh led to the improvement of cardiac pump functions. In 2D echocardiography, post-MI rats exhibited impaired LV systolic function [percent fractional shortening (FS)] and enlarged LV end-systolic diameter (LVESD) compared to the controls at baseline (Fig. 6C). Electrical stimulations with the epicardial mesh significantly reduced the LVESD and increased FS by 51% in post-MI rats (to 33.3 ± 1.98%) but did not restore FS to average control levels of 52% (table S1).

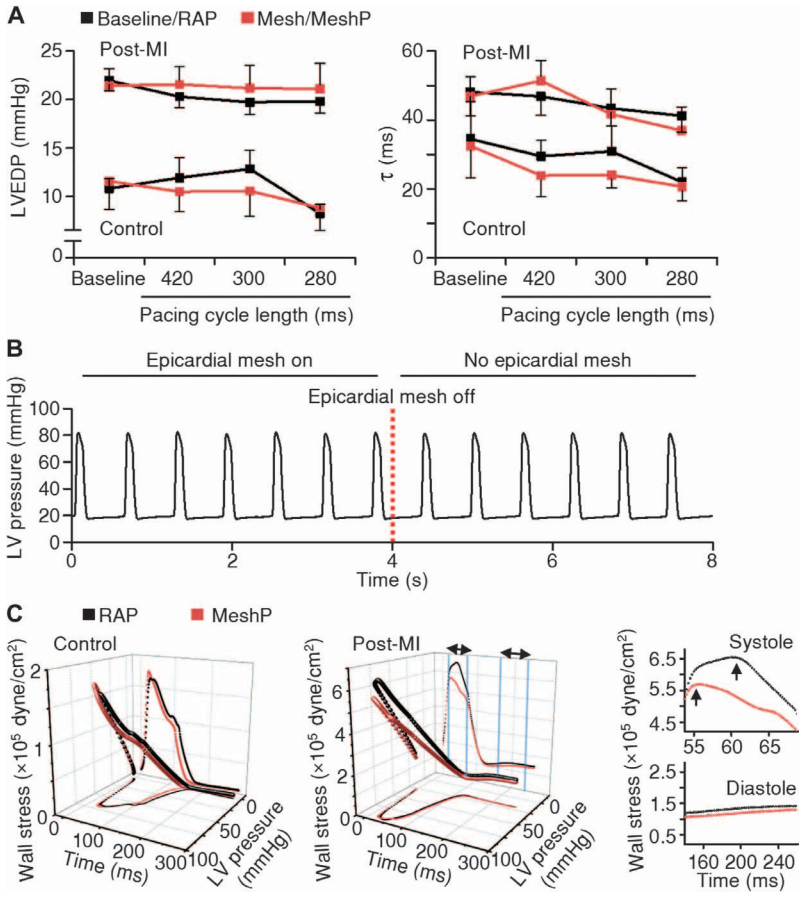

Fig. 5. Hemodynamic and structural effects of electromechanical cardioplasty. (**A**) Effect of the epicardial mesh on diastolic function (LVEDP and τ) in control and 8-week post-MI rats. *P* values were determined by the linear mixed model between sinus rhythm at baseline and sinus rhythm during device implantation, between right atrial pacing (RAP) and mesh pacing (MeshP), and between all individual cycle lengths. All *P* values, including overall *P* value, were statistically insignificant. Data are means ± SEM (n = 5). (**B**) LV pressure before and after removing the epicardial mesh in a representative 8-week post-MI rat. (**C**) LV wall stress-pressure loop during one cardiac cycle. Longitudinal wall stress was derived from simultaneous recordings of LV pressure and myocardial strains during RAP and MeshP at the same cycle length of 280 ms. Data are representative of a control and an 8-week post-MI rat.

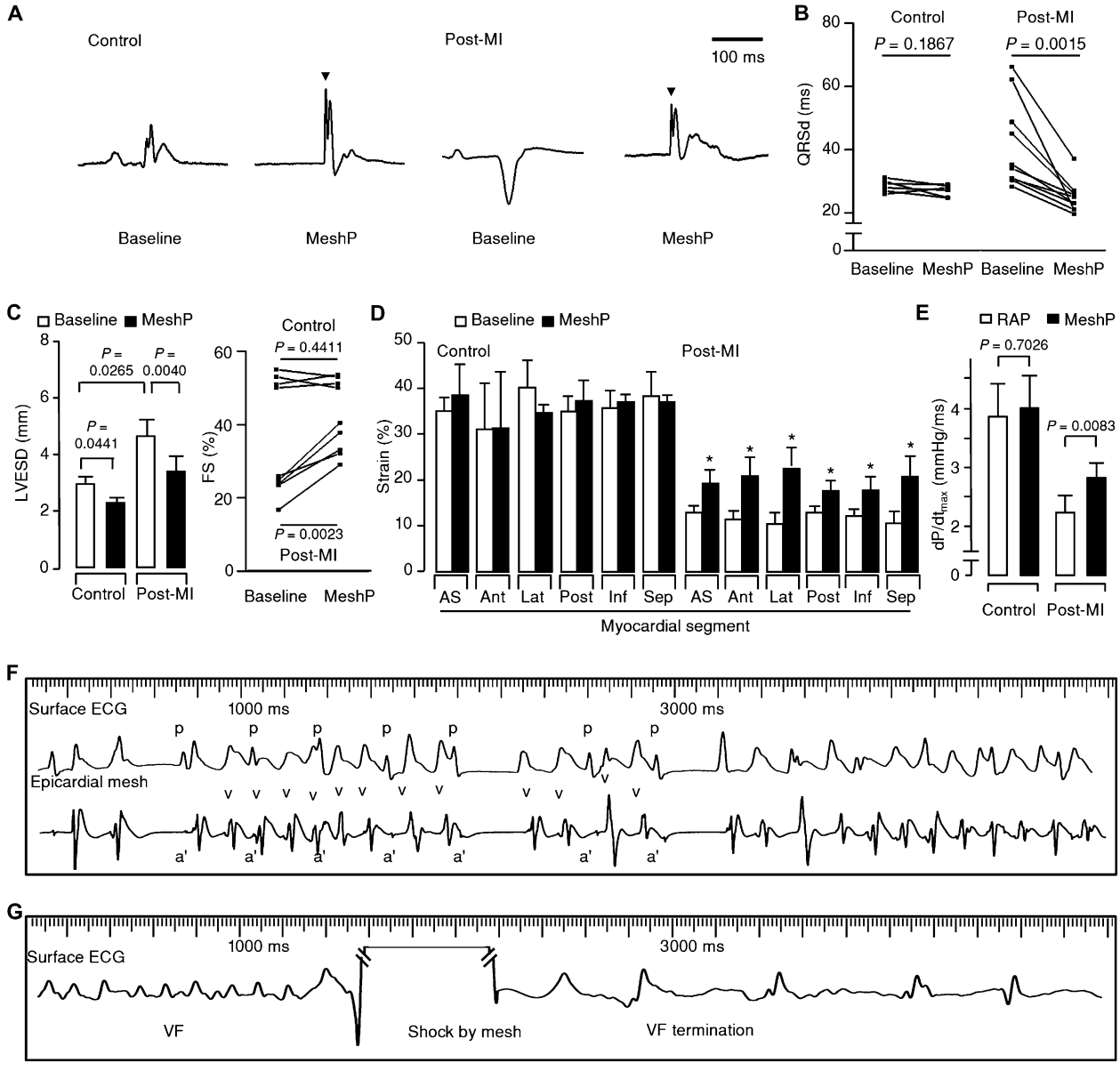

Fig. 6. The effect of electrical stimulation on cardiac electrical and mechanical function and defibrillation function by the epicardial mesh. (**A**) Representative p-QRS-T complexes during sinus rhythm (baseline) and electrical pacing by the epicardial mesh (MeshP) in control and 8-week post-MI hearts. (**B**) Effect of MeshP on total ventricular activation time [QRS durations (QRSd)] in control ($n = 8$) and 8-week post-MI rats ($n = 10$). *P* values were determined by paired Student's *t* test. (**C**) Comparison of LVESD and systolic function (% FS) in control ($n = 4$) and 8-week post-MI ($n = 5$) animals. $^*P < 0.005$, unpaired Student's *t* test; $^{**}P < 0.005$, paired Student's *t* test. (**D**) Speckle tracking of radial strain in control ($n = 5$) and 8-week post-MI hearts ($n = 6$). $^*P < 0.05$ versus respective sinus rhythm, unpaired Student's *t* test. Data are means ± SEM. AS, anteroseptal; Ant, anterior; Lat, lateral; Post, posterior; Inf, inferior; Sep, septal. (**E**) LV contractility index, dP/dt_{max}, during RAP and MeshP in control ($n = 5$) and 8-week post-MI rats ($n = 5$). *P* values were determined by unpaired Student's *t* test. (**F**) Surface ECG depicting occurrence of a wide-QRS tachycardia, identified as nonsustained ventricular tachycardia from the epicardial mesh recording. (**G**) Degeneration to ventricular fibrillation (VF) 3 s later and successful termination with a biphasic electrical shock of 2 J delivered through the epicardial mesh. During all assessments, the cycle length of pacing was 280 ms.

To investigate how electrical stimulation contributes to overall improvement of cardiac pumping functions, we measured peak radial strain of individual segments of the LV chamber wall during electrical stimulation by the epicardial mesh. In control rats, myocardial strain of six LV segments was unchanged by epicardial mesh pacing at a cycle length of 280 ms (Fig. 6D and table S2). In post-MI rats, depressed strains of each LV segment were significantly improved by electrical stimulations at the cycle length of 280 ms (Fig. 6D and table S2). Contractility (dP/dt_{max}) was also improved by the epicardial mesh pacing compared to right atrial pacing (Fig. 6E and table S3). These data indicate that electrical stimulation through the epicardial mesh improves systolic function and contractility by

increasing myocardial strain of individual segments as well as synchronous activity.

Last, the epicardial mesh demonstrated the capability to detect and terminate abnormal electrical activities such as ventricular tachycardia and ventricular fibrillation, both of which occurred spontaneously in the post-MI heart (Fig. 6, F and G). A biphasic electrical shock of 2 J delivered through the epicardial mesh successfully terminated ventricular fibrillation, demonstrating its potential use for both pacing and defibrillation in a future clinical setting.

Biocompatibility of the epicardial mesh and alternative gold-passivated mesh

Before translation, we tested the cellular toxicity and inflammatory reaction of the LE-AgNW/SBS. The ratio of 65:35 of LE-AgNW/SBS revealed minimal adverse reaction in human acute monocytic leukemia cells (THP-1), human umbilical vein endothelial cells (HUVEC), human lung carcinoma cells (A549), and rat myoblasts (H9C2), whereas the 90:10 formulation significantly reduced cell viability in these cell lines (fig. S6A). The mesh made of LE-AgNW/SBS (63:35 ratio) was then implanted in one rat heart and in the skeletal muscles of three rats (abdominal rectus muscle in two rats and femoral muscle in one rat; Fig. 7B and fig. S6, B and C). Histology 3 weeks after implant revealed relatively minimal inflammatory infiltrates (fig. S6D).

We also looked into gold-coated LE-AgNW/SBS meshes that might be more desirable in humans, owing to inherent inert properties (*22*). Therefore, we passivated the surface of LE-AgNW/SBS with a gold thin film deposited by thermal evaporation (Fig. 7A). Inductively coupled plasma mass spectrometry analysis showed that silver ions did not leach out from the gold-coated mesh, but not more so than the regular mesh (fig. S7A). The cytotoxicity test demonstrated better biocompatibility in the Au-coated mesh than in the bare LE-AgNW/SBS mesh in three different cell lines in vitro: A549, HUVEC, and a mouse cardiac muscle cell line, HL-1 (fig. S7B). Hematoxylin and eosin staining and macrophage assay of a rat skeletal muscle also revealed less inflammatory infiltrate in the Au-coated LE-AgNW/SBS mesh (Fig. 7B and fig. S7C). Furthermore, the electrical properties of the Au-coated LE-AgNW/SBS mesh were the same as those of the LE-AgNW/SBS mesh under mechanical deformation (Fig. 7C); thus, the Au-coated LE-AgNW/SBS mesh exhibited clear cardiac electrical activity in control rat in vivo (fig. S7D).

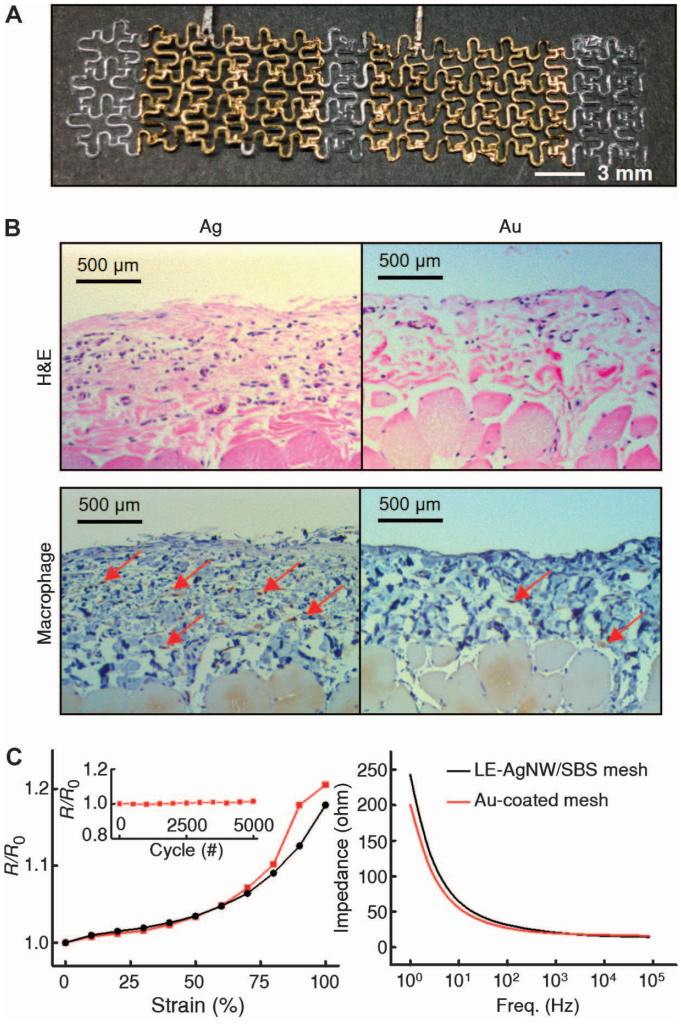

Fig. 7. Biocompatibility of the gold-coated device. (**A**) Photograph of the Au-coated epicardial mesh. (**B**) Histology 3 weeks after the implantation of the epicardial mesh and Au-coated epicardial mesh in rat skeletal muscles. Hematoxylin and eosin (H&E) staining and immunohistochemistry for macrophage. The arrows indicate macrophages. (**C**) Electrical properties. Resistance change under mechanical stretching (left), cyclic resistance behavior under 15% strain (inset), and impedance (right).

DISCUSSION

Here, we introduce an elasto-conductive electrode composed of a silver nanowire–polymer (LE-AgNW/SBS) nanocomposite that is able to conform to the rodent heart and deliver electrical impulses to restore function after MI. The 1D structure of metal nanowires formed a highly conducting electrical network, whereas the SBS rubber acted as a binder to maintain the mechanical elasticity. Electromechanical cardioplasty using the elasto-conductive epicardial mesh improved systolic function by acting as a global epicardial pacemaker to activate the entire ventricular myocardium simultaneously and reduced host myocardial wall stress by acting as a structural component but did not impede ventricular relaxations. All these effects improved cardiac pumping functions in a rodent MI model.

In diseased myocardium, abnormal electrical conduction occurs as a result of impaired muscle-to-muscle conduction as well as disruption to Purkinje fibers. Biventricular pacing was designed to reduce the discoordination of contraction in diseased hearts. However, electrical stimulation by only two point electrodes on both ventricles may be too localized to completely restore the global synchronous contractions. Therefore, we sought to make an artificial Purkinje fiber–like system encircling the outer shell of the heart to maximize synchronous contraction, similar to the mesh-like endocardial Purkinje system in the human ventricles. We also incorporated a defibrillation function to abort sudden death from ventricular arrhythmias. Such device represents a major improvement on the goal of resynchronization, because it restores native activation times and could not be limited by coronary sinus venous anatomy, native QRS width, or LV scar. Furthermore, the potential candidates eligible for biventricular pacing therapy are estimated to be less than 25% of heart failure patients, and only one in four of these potential candidates receives this therapy in an actual

clinical practice (*23*). We believe that electromechanical cardioplasty using an epicardial mesh holds promise for these patients. Two similar heart wraps have been tested in people. Our electromechanical cardioplasty by electrically conductive device consistently improved systolic function in all individual rats, whereas clinical data on cardiac restraint devices and cardiomyoplasty using skeletal muscle showed inconsistent results. However, we would need to investigate this consistency for longer periods of time in the animals and also test in larger animals with spontaneous arrhythmias to comment on survival and prevention of arrhythmic events. For future clinical applications, a percutaneous or surgical technique to gain access to the pericardial space and deploy the cardiac mesh safely and effectively in humans must be developed.

Another advantage of our device is the ability to confer the functions of a structural component on the diseased heart. The elasticity of the epicardial mesh is almost identical to the epicardium, enabling integration with the heart. Tissue engineering, such as cardiac slice transplantation, aims to boost contractile function and reduce stress of the host myocardium by sharing cardiac load with the introduced tissue. However, transplanted cell sheets composed of rat neonatal cardiomyocytes have demonstrated poor survival in rat hearts (14% survival of transplanted cells in infarcted hearts) (*24*, *25*). Taking a different approach, we designed an epicardium-like device that alleviates wall stress by integrating with the host myocardium. Owing to the low elastic modulus of the entire patterned system, the conformal surface contact on the moving heart could be achieved, minimizing the impedance between the mesh electrode and the heart surface (*9*, *26*, *27*) and increasing the adhesion to the heart (*27*). Thus, the mesh recorded ECGs with a high signal-to-noise ratio and stimulated the heart with low threshold current even under cardiac motion.

The customized design of the epicardial mesh allowed adjustable electrical/mechanical properties to the specific heart size and shape. In the past, cardiac support devices, such as a woven polyester jacket and a nitinol mesh placed around the heart, were used in patients with severe heart failure. These clinical studies demonstrated prevention of further dilatation of the LV, promotion of reverse cardiac remodeling, and improvement in symptoms (*6*, *28*), which was likely attributable to reduced wall stress (*29*). The epicardial serpentine mesh also showed a beneficial effect to reduce wall stress in a postinfarct rat heart without worsening diastolic function.

The current study has several limitations. We evaluated the acute response to electromechanical cardioplasty and did not assess long-term effects, mainly because of the large size of the pulse generator in comparison with the whole body of a rat. Although we identified a remarkably beneficial effect on systolic function by electromechanical cardioplasty, long-term response cannot be assured. The correlation of acute changes in dP/dt_{max} with long-term response to cardiac resynchronization therapy has been controversial in clinical data (*30*). Long-term beneficial and adverse effects should be performed in the future. Electromechanical cardioplasty was designed to simultaneously activate the entire epicardium of each ventricle through electrical flow from large dipoles on each side of the LV and RV. Because electrical flow may interact with the blood pool in the ventricular cavities with unknown consequences, it is possible that a version that activates the ventricles using a large number of individual electrical channels in a manner similar to endocardial activation by the Purkinje network may be superior (*31*). Last, epicardial mesh pacing in this experiment was performed without AV synchronization owing to technical difficulty specific to the size of rats. The epicardial mesh pacing without AV synchronization, however, was superior to the baseline or atrial pacing with AV synchronization in post-MI rats, implying that VV synchronization has a much bigger effect on improving hemodynamics than AV synchronization. However, the effort to optimize synchronous contraction of atria and ventricles should be made in clinical application, which is expected to bring better improvement in cardiac hemodynamics.

Our organ-specific therapeutic device with a structure/function-inspired design can extend its application to various cardiac diseases including sinus node dysfunction and cardiac conduction disease. This technology is expected to be a solid basis for new attempts toward electrical modulation therapy to improve systolic function (*32*), low-energy defibrillators as alternatives to the painful defibrillator systems (*33*), or other novel electrical therapies. Furthermore, it could accelerate advanced applications of organ-specific devices integrated with drug delivery system and cardiac tissue engineering. The next step should be to recreate these results in a large-animal model of MI-induced heart failure and evaluate for long-term performance.

MATERIALS AND METHODS

Study design

The aim of this study was to develop electromechanical cardioplasty by wrapping the epicardial surface of the heart in a mesh made of a nanocomposite of LE-AgNW/SBS. The device was designed to have an elastic modulus identical to that of the myocardium. Computer simulations estimated the effect of the epicardial mesh on cardiac hemodynamics. For in vivo experiments, rats were randomly assigned to control and MI groups. Treatment conditions were blinded during all experimental processes. On the basis of our previous experiences with the post-MI model, group sizes were determined; at least six rats were required to identify scar formation at 8 weeks after infarction because mortality is about 50% during an 8-week follow-up period. At 8 weeks after infarction, we evaluated the effect of electrical stimulation with the epicardial mesh device on total ventricular activation time, left ventricular function, myocardial wall stress, and LV pressure.

Large-scale synthesis and ligand exchange reaction of AgNW

To synthesize AgNW, a modified $CuCl_2$-mediated polyol process was used (*34*). Eight hundred microliters of 4 mM copper chloride solution ($CuCl_2{\cdot}2H_2O$, 99%; Strem Chemicals Inc.) was added to 130 ml of 0.034 M PVP (average molecular weight, 55,000; Aldrich) solution in an oil bath (153°C), and then 30 ml of 0.094 M silver nitrate ($AgNO_3$, >99% purity, Strem Chemicals Inc.) in ethylene glycol solution was injected into the reaction mixture. The synthesis reaction lasted for 1 hour. The reaction solution was diluted with acetone and centrifuged at 2000 rpm for 10 min. This centrifugation procedure was repeated twice. Next, 0.3 g of synthesized AgNW was dispersed in 54 ml of dimethylformamide (DMF), and 6 ml of 0.1 M $NOBF_4$ in DMF was added to the AgNW solution. After 5 min of gentle shaking, hexylamine in hexane (HAm) was added to the reaction solution. The synthesized LE-AgNW solution was diluted with ethanol and centrifuged at 2000 rpm. The LE-AgNW was dispersed in 6 ml of toluene.

Fabrication of the mesh electrode

LE-AgNW/SBS (Kumho KTR-101, Kumho Petrochemical) solution was poured on the serpentine-shaped PDMS mold. The remaining solution

on the top of the mold was removed with a blade. The molded solution was dried slowly at 45°C. The LE-AgNW/SBS solution was applied selectively on the bottom of PDMS mold to fabricate the epicardial mesh electrodes that are applied to the heart (fig. S2). Additional SBS solution was poured in the mold to encapsulate the LE-AgNW/SBS layer.

Experimental MI animal model

All animal experiments were approved by the Committee for Care and Use of Laboratory Animals, Yonsei University College of Medicine, and performed in accordance with the *Guidelines and Regulations for Animal Care*. MI was produced in male Sprague-Dawley rats (320 to 430 g) by a permanent LAD ligation. Briefly, after anesthesia with ketamine (10 mg/kg) and xylazine (5 mg/kg), the hearts were exteriorized by opening the chest with sternotomy. Rats that expired during the procedure were excluded from mortality calculation. On the eighth week after permanent LAD ligation, rats were intubated and placed on a rodent ventilator (Hugo Sachs Elektronik-Harvard Apparatus, March-Hugstetten) under zoletil (20 mg/kg) and xylazine (5 mg/kg) anesthesia. Midsternotomy was then performed to expose the hearts, and the epicardial mesh was implanted.

Surface electrocardiography and electrophysiological studies

Surface six-lead ECG (lead II is shown in figures) was continuously recorded along with all intracardiac electrograms and stored in the amplifier/recorder system (Pruka CardioLab IT System, GE Healthcare). The sampling rate was 4 kHz. R-R intervals, QRS durations, and QT intervals were measured as described previously (*35*, *36*). For the QTc interval measurement, Bazett's formula was used (*37*). All parameters were measured twice by a cardiologist (H.J.H.) and a blinded investigator. The intraobserver variability was <10% for the cardiologists and electrophysiologists. Intracardiac electrograms were obtained from an epicardial mesh electrode and a 4F bipolar electrode catheter (2-mm interval; St. Jude Medical). Stimulation was performed at twice the pacing threshold of rectangular stimulus pulses with duration of 2 ms by a programmable digital stimulator (Bloom DTU 215, Fisher Medical Technologies) (average pacing threshold, 1.1 ± 0.2 mA). Ventricular tachycardia was defined as at least four ventricular beats and identified on the basis of atrioventricular dissociation on the intracardiac electrogram.

Statistical analysis

Data were expressed as means ± SEM for continuous variables and as proportions for categorical variables. For parametric variables, statistical analyses of pairs of groups and samples were conducted with paired and unpaired two-tailed Student's *t* test, respectively. A linear mixed model was used to account for repeated measurements in each group. In the linear mixed model, animals were included as random effects, and conditions (sinus rhythm, presence or absence of mesh), pacing (420, 320, and 280 ms), and interactions were treated as fixed effects. Appropriate contrasts were selected to analyze differences between pacing levels and conditions. Differences in end-diastolic pressure, dP/dt_{max}, and τ values between groups at sinus rhythm and each pacing cycle length (420, 320, and 280 ms) were compared. The association between heart rates and QRS durations was analyzed using the Pearson correlation test. $P < 0.05$ was considered to represent a statistically significant difference. Statistical analysis was performed using the SPSS package for Windows (version 18.0; SPSS Inc). All statistical analyses were performed by two-sided tests.

SUPPLEMENTARY MATERIALS

www.sciencetranslationalmedicine.org/cgi/content/full/8/344/344ra86/DC1
Materials and Methods
Fig. S1. Characterization of LE-AgNW and LE-AgNW/SBS nanocomposite.
Fig. S2. PDMS mold fabrication process for the epicardial mesh.
Fig. S3. Electrical stimulation by the epicardial mesh.
Fig. S4. The relation of heart rates to QRS durations, and epicardial mesh pacing at 90% of the baseline cycle lengths.
Fig. S5. Speckle tracking radial strain.
Fig. S6. Evaluation of cytotoxicity of the LE-AgNW/SBS film.
Fig. S7. Feasibility and safety test of the gold-coated epicardial mesh.
Table S1. Echocardiographic data in controls and 8-week post-MI rats.
Table S2. Speckle tracking radial strain data in control and 8-week post-MI hearts.
Table S3. LV contractility index, dP/dt_{max}, in controls and 8-week post-MI rats.
Movie S1. Manual testing of the elasticity of the epicardial mesh.
References (*38*–*46*)

REFERENCES AND NOTES

1. M. E. Josephson, *Clinical Cardiac Electrophysiology: Techniques and Interpretations* (Wolters Kluwer Health/Lippincott Williams & Wilkins, Philadelphia, PA, 2008).
2. A. S. L. Tang, G. A. Wells, M. Talajic, M. O. Arnold, R. Sheldon, S. Connolly, S. H. Hohnloser, G. Nichol, D. H. Birnie, J. L. Sapp, R. Yee, J. S. Healey, J. L. Rouleau; Resynchronization–Defibrillation for Ambulatory Heart Failure Trial Investigators, Cardiac-resynchronization therapy for mild-to-moderate heart failure. *N. Engl. J. Med.* **363**, 2385–2395 (2010).
3. WRITING COMMITTEE MEMBERS, C. W. Yancy, M. Jessup, B. Bozkurt, J. Butler, D. E. Casey Jr., M. H. Drazner, G. C. Fonarow, S. A. Geraci, T. Horwich, J. L. Januzzi, M. R. Johnson, E. K. Kasper, W. C. Levy, F. A. Masoudi, P. E. McBride, J. J. V. McMurray, J. E. Mitchell, P. N. Peterson, B. Riegel, F. Sam, L. W. Stevenson, W. H. W. Tang, E. J. Tsai, B. L. Wilkoff; American College of Cardiology Foundation/American Heart Association Task Force on Practice Guidelines, 2013 ACCF/AHA guideline for the management of heart failure: A report of the American College of Cardiology Foundation/American Heart Association Task Force on practice guidelines. *Circulation* **128**, e240–e327 (2013).
4. R. M. El Oakley, J. C. Jarvis, Cardiomyoplasty. A critical review of experimental and clinical results. *Circulation* **90**, 2085–2090 (1994).
5. M. R. Costanzo, R. J. Ivanhoe, A. Kao, I. S. Anand, A. Bank, J. Boehmer, T. DeMarco, C. M. Hergert, R. G. Holcomb, S. Maybaum, B. Sun, T. A. Vassiliades Jr., B. K. Rayburn, W. T. Abraham, Prospective evaluation of elastic restraint to lessen the effects of heart failure (PEERLESS-HF) trial. *J. Card. Fail.* **18**, 446–458 (2012).
6. D. L. Mann, S. H. Kubo, H. N. Sabbah, R. C. Starling, M. Jessup, J. K. Oh, M. Acker, Beneficial effects of the CorCap cardiac support device: Five-year results from the Acorn Trial. *J. Thorac. Cardiovasc. Surg.* **143**, 1036–1042 (2012).
7. A. S. Rubino, F. Onorati, G. Santarpino, E. Pasceri, G. Santarpia, L. Cristodoro, G. F. Serraino, A. Renzulli, Neurohormonal and echocardiographic results after CorCap and mitral annuloplasty for dilated cardiomyopathy. *Ann. Thorac. Surg.* **88**, 719–725 (2009).
8. G. D. Moon, G.-H. Lim, J. H. Song, M. Shin, T. Yu, B. Lim, U. Jeong, Highly stretchable patterned gold electrodes made of Au nanosheets. *Adv. Mater.* **25**, 2707–2712 (2013).
9. L. Xu, S. R. Gutbrod, A. P. Bonifas, Y. Su, M. S. Sulkin, N. Lu, H.-J. Chung, K.-I. Jang, Z. Liu, M. Ying, C. Lu, R. C. Webb, J.-S. Kim, J. I. Laughner, H. Cheng, Y. Liu, A. Ameen, J.-W. Jeong, G.-T. Kim, Y. Huang, I. R. Efimov, J. A. Rogers, 3D multifunctional integumentary membranes for spatiotemporal cardiac measurements and stimulation across the entire epicardium. *Nat. Commun.* **5**, 3329 (2014).
10. K.-Y. Chun, Y. Oh, J. Rho, J.-H. Ahn, Y.-J. Kim, H. R. Choi, S. Baik, Highly conductive, printable and stretchable composite films of carbon nanotubes and silver. *Nat. Nanotechnol.* **5**, 853–857 (2010).
11. T. Sekitani, Y. Noguchi, K. Hata, T. Fukushima, T. Aida, T. Someya, A rubberlike stretchable active matrix using elastic conductors. *Science* **321**, 1468–1472 (2008).
12. L. Hu, H. S. Kim, J.-Y. Lee, P. Peumans, Y. Cui, Scalable coating and properties of transparent, flexible, silver nanowire electrodes. *ACS Nano* **4**, 2955–2963 (2010).
13. P. Lee, J. Lee, H. Lee, J. Yeo, S. Hong, K. H. Nam, D. Lee, S. S. Lee, S. H. Ko, Highly stretchable and highly conductive metal electrode by very long metal nanowire percolation network. *Adv. Mater.* **24**, 3326–3332 (2012).
14. J. M. Yang, S. C. Tsai, Biocompatibility of epoxidized styrene–butadiene–styrene block copolymer membrane. *Mater. Sci. Eng. C* **30**, 1151–1156 (2010).
15. J. E. Kennedy, C. L. Higginbotham, in *Biomedical Engineering, Trends in Materials Science* (InTech, Crotia, 2011), pp. 465–484.
16. Y. Kim, J. Zhu, B. Yeom, M. Di Prima, X. Su, J.-G. Kim, S. J. Yoo, C. Uher, N. A. Kotov, Stretchable nanoparticle conductors with self-organized conductive pathways. *Nature* **500**, 59–63 (2013).

17. S. Choi, J. Park, W. Hyun, J. Kim, J. Kim, Y. B. Lee, C. Song, H. J. Hwang, J. H. Kim, T. Hyeon, D.-H. Kim, Stretchable heater using ligand-exchanged silver nanowire nanocomposite for wearable articular thermotherapy. *ACS Nano* **9**, 6626–6633 (2015).
18. D. L. Mann, *Braunwald's Heart Disease: A Textbook of Cardiovascular Medicine* (W.B. Saunders Company Limited, 2014).
19. P. Faria, M. Hallett, P. C. Miranda, A finite element analysis of the effect of electrode area and inter-electrode distance on the spatial distribution of the current density in tDCS. *J. Neural Eng.* **8**, 066017 (2011).
20. J. E. Stevens-Lapsley, J. E. Balter, P. Wolfe, D. G. Eckhoff, R. S. Schwartz, M. Schenkman, W. M. Kohrt, Relationship between intensity of quadriceps muscle neuromuscular electrical stimulation and strength recovery after total knee arthroplasty. *Phys. Ther.* **92**, 1187–1196 (2012).
21. L. H. Opie, *Heart Physiology: From Cell to Circulation* (Lippincott Williams & Wilkins, Philadelphia, PA, 2004).
22. R. A. Sperling, P. Rivera Gil, F. Zhang, M. Zanella, W. J. Parak, Biological applications of gold nanoparticles. *Chem. Soc. Rev.* **37**, 1896–1908 (2008).
23. J. De Sutter, C. Weytjens, N. Van de Veire, F. Provenier, B. Vande Kerckhove, A.-M. Willems, N. De Laet, G. Van Camp, Prevalence of potential cardiac resynchronization therapy candidates and actual use of cardiac resynchronization therapy in patients hospitalized for heart failure. *Eur. J. Heart Fail.* **13**, 412–415 (2011).
24. J. Riegler, A. Gillich, Q. Shen, J. D. Gold, J. C. Wu, Cardiac tissue slice transplantation as a model to assess tissue-engineered graft thickness, survival, and function. *Circulation* **130**, S77–S86 (2014).
25. K. E. A. van der Bogt, A. Y. Sheikh, S. Schrepfer, G. Hoyt, F. Cao, K. J. Ransohoff, R.-J. Swijnenburg, J. Pearl, A. Lee, M. Fischbein, C. H. Contag, R. C. Robbins, J. C. Wu, Comparison of different adult stem cell types for treatment of myocardial ischemia. *Circulation* **118**, S121–S129 (2008).
26. D.-H. Kim, N. Lu, R. Ma, Y.-S. Kim, R.-H. Kim, S. Wang, J. Wu, S. M. Won, H. Tao, A. Islam, K. J. Yu, T.-i. Kim, R. Chowdhury, M. Ying, L. Xu, M. Li, H.-J. Chung, H. Keum, M. McCormick, P. Liu, Y.-W. Zhang, F. G. Omenetto, Y. Huang, T. Coleman, J. A. Rogers, Epidermal electronics. *Science* **333**, 838–843 (2011).
27. J. Viventi, D.-H. Kim, J. D. Moss, Y.-S. Kim, J. A. Blanco, N. Annetta, A. Hicks, J. Xiao, Y. Huang, D. J. Callans, J. A. Rogers, B. Litt, A conformal, bio-interfaced class of silicon electronics for mapping cardiac electrophysiology. *Sci. Transl. Med.* **2**, 24ra22 (2010).
28. C. T. Klodell Jr., J. M. Aranda Jr., D. C. McGiffin, B. K. Rayburn, B. Sun, W. T. Abraham, W. E. Pae Jr., J. P. Boehmer, H. Klein, C. Huth, Worldwide surgical experience with the Paracor HeartNet cardiac restraint device. *J. Thorac. Cardiovasc. Surg.* **135**, 188–195 (2008).
29. J. F. Wenk, L. Ge, Z. Zhang, D. Mojsejenko, D. D. Potter, E. E. Tseng, J. M. Guccione, M. B. Ratcliffe, Biventricular finite element modeling of the Acorn CorCap Cardiac Support Device on a failing heart. *Ann. Thorac. Surg.* **95**, 2022–2027 (2013).
30. C. Madias, R. G. Trohman, Cardiac resynchronization Therapy: the state of the art. *Expert Rev. Cardiovasc. Ther.* **12**, 573–587 (2014).
31. C. Pappone, Ž. Ćalović, G. Vicedomini, A. Cuko, L. C. McSpadden, K. Ryu, E. Romano, M. Saviano, M. Baldi, A. Pappone, C. Ciaccio, L. Giannelli, B. Ionescu, A. Petretta, R. Vitale, A. Fundaliotis, L. Tavazzi, V. Santinelli, Multipoint left ventricular pacing improves acute hemodynamic response assessed with pressure-volume loops in cardiac resynchronization therapy patients. *Heart Rhythm* **11**, 394–401 (2014).
32. A. R. Lyon, M. A. Samara, D. S. Feldman, Cardiac contractility modulation therapy in advanced systolic heart failure. *Nat. Rev. Cardiol.* **10**, 584–598 (2013).
33. A. H. Janardhan, W. Li, V. V. Fedorov, M. Yeung, M. J. Wallendorf, R. B. Schuessler, I. R. Efimov, A novel low-energy electrotherapy that terminates ventricular tachycardia with lower energy than a biphasic shock when antitachycardia pacing fails. *J. Am. Coll. Cardiol.* **60**, 2393–2398 (2012).
34. K. E. Korte, S. E. Skrabalak, Y. Xia, Rapid synthesis of silver nanowires through a CuCl- or $CuCl_2$-mediated polyol process. *J. Mater. Chem.* **18**, 437–441 (2008).
35. C. I. Berul, M. J. Aronovitz, P. J. Wang, M. E. Mendelsohn, In vivo cardiac electrophysiology studies in the mouse. *Circulation* **94**, 2641–2648 (1996).
36. G. F. Mitchell, A. Jeron, G. Koren, Measurement of heart rate and Q-T interval in the conscious mouse. *Am. J. Physiol.* **274**, H747–H751 (1998).
37. H. C. Bazett, An Analysis of the time-relations of electrocardiograms. *Ann. Noninvasive Electrocardiol.* **2**, 177–194 (1997).
38. Y. Xia, G. M. Whitesides, Soft lithography. *Angew. Chem., Int. Ed.* **37**, 550–575 (1998).
39. P. G. Young, T. B. H. Beresford-West, S. R. L. Coward, B. Notarberardino, B. Walker, A. Abdul-Aziz, An efficient approach to converting three-dimensional image data into highly accurate computational models. *Philos. Trans.: Math., Phys. Eng. Sci.* **366**, 3155–3173 (2008).
40. V. Y. Wang, H. I. Lam, D. B. Ennis, B. R. Cowan, A. A. Young, M. P. Nash, Modelling passive diastolic mechanics with quantitative MRI of cardiac structure and function. *Med. Image Anal.* **13**, 773–784 (2009).
41. S. Klotz, M. L. Dickstein, D. Burkhoff, A computational method of prediction of the end-diastolic pressure–volume relationship by single beat. *Nat. Protoc.* **2**, 2152–2158 (2007).
42. J. Wong, E. Kuhl, Generating fibre orientation maps in human heart models using Poisson interpolation. *Comput. Methods Biomech. Biomed. Engin.* **17**, 1217–1226 (2014).
43. R. Q. Migrino, X. Zhu, N. Pajewski, T. Brahmbhatt, R. Hoffmann, M. Zhao, Assessment of segmental myocardial viability using regional 2-dimensional strain echocardiography. *J. Am. Soc. Echocardiogr.* **20**, 342–351 (2007).
44. J. A. Chirinos, P. Segers, A. K. Gupta, A. Swillens, E. R. Rietzschel, M. L. De Buyzere, J. N. Kirkpatrick, T. C. Gillebert, Y. Wang, M. G. Keane, R. Townsend, V. A. Ferrari, S. E. Wiegers, M. St. John Sutton, Time-varying myocardial stress and systolic pressure-stress relationship: Role in myocardial-arterial coupling in hypertension. *Circulation* **119**, 2798–2807 (2009).
45. R. M. Lang, M. Bierig, R. B. Devereux, F. A. Flachskampf, E. Foster, P. A. Pellikka, M. H. Picard, M. J. Roman, J. Seward, J. Shanewise, S. Solomon, K. T. Spencer, M. St John Sutton, W. Stewart; American Society of Echocardiography's Nomenclature and Standards Committee, Task Force on Chamber Quantification, American College of Cardiology Echocardiography Committee, American Heart Association, European Association of Echocardiography, European Society of Cardiology, Recommendations for chamber quantification. *Eur. J. Echocardiogr.* **7**, 79–108 (2006).
46. D. M. Regen, Calculation of left ventricular wall stress. *Circ. Res.* **67**, 245–252 (1990).

Acknowledgments: We acknowledge the assistance of J. K. Kim for the surgical procedure, J. Park for the pressure loop recording, H. S. Lee for the statistical analysis, and I. Shin for the 3D reconstructed heart image. **Funding:** This work was supported by IBS-R006-D1. N. Lu acknowledges the U.S. NSF Civil, Mechanical and Manufacturing Innovation (CMMI) award under grant no. 1301335. S.R. acknowledges use of computational resources at the Center of Cardiovascular Simulation–Institute of Computational Engineering and Sciences (University of Texas at Austin). **Author contributions**: J.P., S.C., T.H., D.-H.K., and H.J.H. designed and performed the experiments. J.P., S.C., S.-Y.L., H.R.C., S.H.C., and H.-H. performed the animal experiments. J.P. and K.-W.K. performed statistical analysis. S.R., J.S., S.Y., M.S., and N. Lu performed computer simulation. K.S. and S.J.K. prepared cell lines and evaluated cellular toxicity in vitro. C.L., K.-W.K., H.-J.L., and N. Lee analyzed medical data and images. J.P., S.C., P.S., W.H., S.J., T.H., D.-H.K., and H.H. performed materials analysis and device experiments. J.P., S.C., A.H.J., N. Lu, M.E.J., T.H., D.-H.K., and H.J.H. wrote the paper. **Competing interests:** The authors declare that they have no competing interests. **Data and materials availability:** All data and materials are available.

Submitted 12 November 2015
Accepted 3 June 2016
Published 22 June 2016
10.1126/scitranslmed.aad8568

Citation: J. Park, S. Choi, A. H. Janardhan, S.-Y. Lee, S. Raut, J. Soares, K. Shin, S. Yang, C. Lee, K.-W. Kang, H. R. Cho, S. J. Kim, P. Seo, W. Hyun, S. Jung, H.-J. Lee, N. Lee, S. H. Choi, M. Sacks, N. Lu, M. E. Josephson, T. Hyeon, D.-H. Kim, H. J. Hwang, Electromechanical cardioplasty using a wrapped elasto-conductive epicardial mesh. *Sci. Transl. Med.* **8**, 344ra86 (2016).

Science Translational Medicine
AAAS

Electromechanical cardioplasty using a wrapped elasto-conductive epicardial mesh

Jinkyung Park, Suji Choi, Ajit H. Janardhan, Se-Yeon Lee, Samarth Raut, Joao Soares, Kwangsoo Shin, Shixuan Yang, Chungkeun Lee, Ki-Woon Kang, Hye Rim Cho, Seok Joo Kim, Pilseon Seo, Wonji Hyun, Sungmook Jung, Hye-Jeong Lee, Nohyun Lee, Seung Hong Choi, Michael Sacks, Nanshu Lu, Mark E. Josephson, Taeghwan Hyeon, Dae-Hyeong Kim and Hye Jin Hwang (June 22, 2016)
Science Translational Medicine **8** (344), 344ra86. [doi: 10.1126/scitranslmed.aad8568]

Editor's Summary

An electromechanical hug for the heart

Heart failure can be treated by pacemakers to keep the beats in rhythm, but pacemakers apply electrical stimulation at specific points and do not provide comprehensive coverage of the entire organ. Park and colleagues therefore devised an electric mesh that wraps around the heart to deliver electrical impulses to the whole ventricular myocardium. The heart wrap was made from silver nanowires embedded in a rubber polymer that could conform to the unique three-dimensional anatomy of different hearts. In rats that had a heart attack, the mesh integrated structurally and electrically with the myocardium and exerted beneficial effects, including preserved diastolic relaxation, reduced wall stress, and improved cardiac contractile function. The mesh also terminated induced ventricular arrhythmia, acting as an epicardial defibrillator. Such epicardial meshes have been tested in clinical trials before and were effective in preventing ventricular remodeling but showed controversial results in long-term survival. The authors hope that their device, which is designed to integrate more faithfully with the heart's structure and electrical conduction system, is more consistent in people.

Science Translational Medicine (print ISSN 1946-6234; online ISSN 1946-6242) is published weekly, except the last week in December, by the American Association for the Advancement of Science, 1200 New York Avenue, NW, Washington, DC 20005.

Science Translational Medicine
AAAS

www.sciencetranslationalmedicine.org/cgi/content/full/8/344/344ra86/DC1

Supplementary Materials for

Electromechanical cardioplasty using a wrapped elasto-conductive epicardial mesh

Jinkyung Park, Suji Choi, Ajit H. Janardhan, Se-Yeon Lee, Samarth Raut, Joao Soares, Kwangsoo Shin, Shixuan Yang, Chungkeun Lee, Ki-Woon Kang, Hye Rim Cho, Seok Joo Kim, Pilseon Seo, Wonji Hyun, Sungmook Jung, Hye-Jeong Lee, Nohyun Lee, Seung Hong Choi, Michael Sacks, Nanshu Lu, Mark E. Josephson, Taeghwan Hyeon,* Dae-Hyeong Kim,* Hye Jin Hwang*

*Corresponding author. Email: hhwang@bidmc.harvard.edu (H.J.H.); dkim98@snu.ac.kr (D.-H.K.); thyeon@snu.ac.kr (T.H.)

Published 22 June 2016, *Sci. Transl. Med.* **8**, 344ra86 (2016)
DOI: 10.1126/scitranslmed.aad8568

The PDF file includes:

Other Supplementary Material for this manuscript includes the following:
(available at www.sciencetranslationalmedicine.org/cgi/content/full/8/344/344ra86/DC1)

Movie S1 (.avi format). Manual testing of the elasticity of the epicardial mesh.

Materials and Methods

Fabrication of PDMS mold for epicardial mesh

We designed the mesh pattern using computer-aided design software system (AutoCAD). The metal mold from this pattern was treated by vapor phase of trichloro(1H,1H,2H,2H-perfluorooctyl)silane (FOTS) to form an anti-sticking self-assembly layer. In order to create the embossing pattern of the serpentine mesh, a certain amount of photo-curable polymer (MINS-301, Minuta Tech) was poured on the treated metal mold. After partial curing with a 30-s exposure to ultraviolet (UV) irradiation, the PUA specimen was easily detachable from the metal mold. The detached specimen was fully cured after 5 h exposure to UV. The cured PUA embossing pattern was also treated with FOTS before casting with polydimethylsiloxane (PDMS) (Sylgard 184, Dow Corning, mixed at 10:1 ratio of pre-polymer and curing agent). PDMS was cured in an oven at 70^{o}C. The PDMS mold fabrication was complete after releasing the PUA embossing pattern from the cast PDMS (*38*).

Resistance and conductivity measurements

Resistance of the epicardial mesh electrode was measured with a parameter analyzer (B1500A, Agilent) while increasing tensile strain from 0 to 50% with an automatic uniaxial stretching stage (Jaeil Optical System). Resistance changes were also measured with a digital multi-meter (NI USB-4065, National Instruments) over repeating stretch-release cycles (15% strain). Electrical conductivity of LE-AgNW/SBS nanocomposite was measured with the four-point probe method (CMT-100MP, AiT).

Stress-strain measurements

Stress-strain curves of LE-Ag/SBS film encapsulated in SBS (approximately 10 mm wide and 30–35 mm long), hyperserpentine mesh (approximately 28 mm wide and 25 mm long), and epicardial mesh (15 mm wide and 40 mm long) were recorded using a tensile mechanical testing system (ESM301, Mark-10, USA). Stress-strain curves of the epicardial tissue specimens were measured using an Instron-5543 electromechanical system (Instron) controlled by the Bluehill software (v3). Sprague-Dawley rats (320 g) were sacrificed according to the relevant guidelines and regulations for animal care, and the hearts were excised and stored in ice-cold Hanks' balanced salt solution (HBSS). The epicardial sheets of the left ventricular (LV) wall were dissected and trimmed into circumferentially oriented rectangular specimens (approximately 7 mm wide, 10 mm long, and 2 mm thick). Specimens were strained at a rate of 10 mm/min until failure.

Cardiac computed tomography (CT)

CT scans for 3D printing were performed using a second-generation dual-source CT (SOMATOM Definition Flash, Siemens Medical Solutions). First, a non-enhanced CT image was obtained to confirm the scan range and the location of the aortic arch for bolus tracking. The scanning ranged from the lung apex to the diaphragm. Next, contrast CT was performed with 2 mL/kg of contrast media (Iopamiro 370, Bracco), which was injected into a tail vein. The initial delay was defined by bolus tracking in the aortic arch, and the scan was automatically initiated 2 s after reaching the threshold of 400 HU. Scanning was performed using the following parameters: high pitch spiral acquisition, 80 kVp, 50 mAs, 64 × 0.6 mm slice collimation, and 330 ms gantry rotation time. The mean scanning time was 0.90 s. CT images were reconstructed

using a slice thickness of 0.75 mm, increment interval of 0.5 mm, and medium-smooth convolution kernel B36f. The field of view was adjusted according to the thorax size.

Computer simulations

High-resolution micro-CT images were segmented, and a 3-dimensional finite element mesh for biventricular geometry below the valve plane was obtained (*39*). The finite element mesh consisted of 48,832 quadratic tetrahedrons for the myocardium and 16,296 quadratic triangular shell elements for the epicardial mesh wrap and film wrap. The total thickness of the shell was set to 88 μm based on the measurement of epicardial mesh samples by scanning electron microscopy. A large deformation, large strain, hybrid formulation was implemented. The anisotropic myocardium was described as an incompressible, hyperelastic, transversely isotropic material (*40*) with parameters fitted to match a normalized end-diastolic pressure-volume relationship (*41*). Fiber directions on the myocardium were generated using Poisson interpolation (*42*). The wrap material behavior was described using different incompressible hyperelastic properties for each case (neo-Hookean with $E = 3\ \mu = 50$ kPa for the epicardial mesh wrap, and 47 MPa for the film wrap). Out-of-plane motion of nodes on the top surface was constrained. A pressure of 90 mmHg was applied on the LV endocardium and $1/8^{th}$ of LV pressure to the RV endocardium. RV pressure does not appreciably affect the LV pressure-volume relation because of the thicker LV wall and smaller RV pressure. There was no relative sliding motion between the sock and the underlying myocardium. To assess the effect of the epicardial mesh on the ventricular chambers, EDPVR was calculated.

Echocardiography

An echocardiograph (Vivid i, GE Healthcare) was used with an 11 MHz M12L-RS linear array transducer. The parasternal short axis of the mid-LV was used for the study. Image depth was 2–2.5 cm with 234–340 frames/s acquisition using second harmonic imaging. ECG gating was used. The method of data acquisition is described in Supplementary Materials.

LV catheterization

LV catheterization was performed for invasive hemodynamics. A Millar Mikro-tip 2 F pressure transducer (model SPR-838, Millar Instruments) was introduced into the LV *via* the apex. Real-time pressure loops were recorded, and all data were analyzed off-line with the PVAN 3.5 software (Millar) by an independent investigator.

Speckle tracking radial strain

Non-Doppler strains were measured using a dedicated software package (EchoPac PC; GE Healthcare) as described previously (*43*). For each cardiac cycle (defined from the peak of the R wave to the following R wave), the endocardial border was manually traced at end-systole. Adequate tracking was verified in real time and corrected by adjusting the region of interest or manually correcting the contour to ensure optimal tracking. The outer border was adjusted to approximate the epicardial contour. The software automatically computed radial strain in 6 segments of the mid-LV throughout the cardiac cycle. End-systole was defined as the time point when the radial strain rate became zero after being positive. Data were analyzed off-line by an independent investigator twice. Intra-observer variability was <10%.

Myocardial wall stress

Two-dimensional echocardiogram (Vivid i, GE Healthcare) was recorded simultaneously with pressure in the LV cavity with a Millar catheter. Data for analysis were collected when the pressure waveform was not distorted by the echocardiographic transducer on the heart. Time-resolved numerical values of radial strain and displacement obtained from the echoPAC software were transferred to Matlab (Mathworks). Longitudinal myocardial stress was also processed in Matlab as shown in the previous study (*44*). The mean of difference of longitudinal wall stresses in systole between right atrial pacing (RAP) and epicardial mesh pacing (MeshP) at the same cycle length of 280 ms was calculated;

$$\text{Mean of difference of wall stresses} = \frac{1}{\Delta t} \sum_{i=0}^{i=\text{end-systole}} \text{RAP wall stress}(t_i) - \text{MeshP wall stress}(t_i)$$

$$\Delta t = t_{\text{end-systole}} - t_o$$

End-systole was defined as the time point when the radial strain rate became zero after being positive. The mean of difference of longitudinal wall stresses during diastole at the above condition was calculated:

$$\text{Mean of difference of wall stresses} = \frac{1}{\Delta t} \sum_{i=\text{end-systole}}^{i=\text{end-diastole}} \text{RAP wall stress}(t_i) - \text{MeshP wall stress}(t_i)$$

$$\Delta t = t_{\text{end-diastole}} - t_{\text{end-systole}}$$

Two-dimensional (2D) echocardiographic measurements

Anatomical M-mode was used to measure left ventricular (LV) internal diameter at diastole (LVIDd) and systole (LVIDs) based on the 2D image of mid-LV. Fractional shortening (FS) was calculated using the following formula:

$$FS = (LVIDd - LVIDs)/LVIDd \times 100\%$$

For circumferential strain measurement of the outer layer of the ventricles, 2D images with well-defined anatomic landmarks, prominent papillary muscles, and anterior and posterior insertion of the right ventricle were selected and transferred to a computer-aided design software system (AutoCAD). Epicardial contour was manually tracked, circumferential length was measured at end-systole and end-diastole, and circumferential strain was calculated.

Micro-computed tomography (μCT)

Because computer simulation of the pressure-volume curve requires high image resolution, we performed heart micro-CT *ex vivo* (SkyScan 1272, Bruker). The following imaging parameters were used: source parameters, 90 kV, 111 μA; image pixel size, 19.84 μm; exposure time, 2291 ms; rotation step, 0.4°; filters, Al 0.5 + Cu 0.038; and scan duration, 36 min. Reconstruction performed with the NRecon V1.6.9.8 software (SkyScan) yielded cross-section images with a pixel size of 1112 x 1112 and slice distance 19.84 μm.

Myocardial wall stress measurement

Average wall thickness in end-diastole (h_{ED}) was calculated as follows (*45*):

$$h_{ED} = \sqrt{A_{EPI}/\pi} - \sqrt{A_{ENDO}/\pi}$$

where A_{EPI} is the epicardial area and A_{ENDO} is the endocardial area. Instantaneous average wall thickness was computed using Lagrangian radial strain:

$$h(t) = h_{ED} \cdot \varepsilon_{RAD}(t)$$

where h(t) is wall thickness at time t and $\epsilon_{RAD}$is average radial strain at time t. Longitudinal myocardial stress (LS) was calculated at each time point during ejection according to (*46*):

$$LS = Pb_m / 2h$$

where P is left ventricular pressure, h is average wall thickness, and b_m is midwall minor semiaxis (radius). Midwall minor semiaxis was calculated as follows:

$$b_m = (b_o - b_c)/(\ln b_o - \ln b_c)$$

where b_o is minor semiaxis (radius) of the outer (epicardial) myocardial shell and b_c is minor semiaxis of the ventricular cavity.

Histological analysis

Hearts were fixed in 10% formalin solution for 24 h at 4°C. Paraffin blocks were made, and 2-µm slides were prepared for Masson's trichrome staining, and 4-µm-thick tissue sections were prepared for macrophage assays. The sections were deparaffinized in xylene and hydrated by immersing in a series of graded ethanol. Antigen retrieval was performed in a microwave by placing the sections in epitope retrieval solution (0.01 M citrate buffer, pH 6.0) for 20 minutes; endogenous peroxidase was inhibited by immersing the sections in 0.3% hydrogen peroxide for 10 minutes. Sections were then incubated with primary rabbit poly antibody to F4/80 (Santa Cruz) for macrophages. Staining for the detection of bound antibody was evaluated by DAB

Supplementary Figures

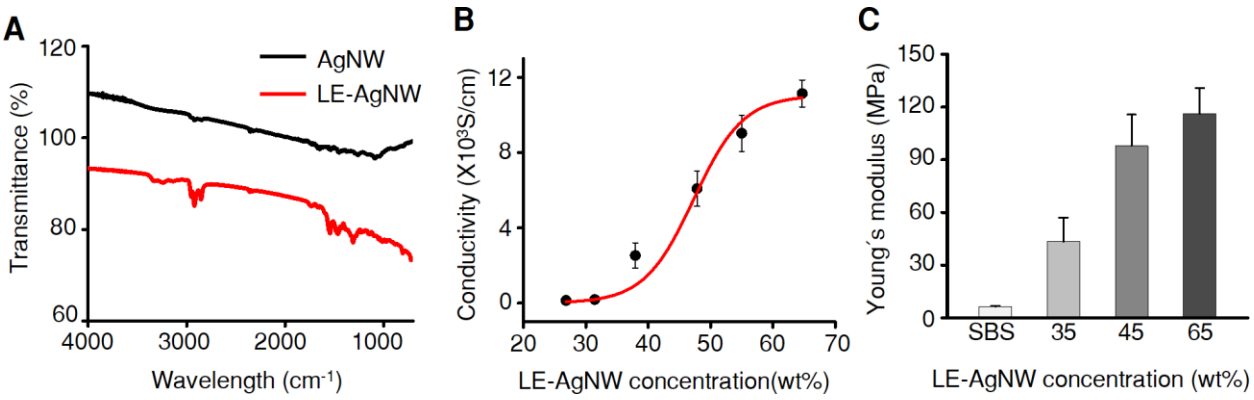

Fig. S1. Characterization of LE-AgNW and LE-AgNW/SBS nanocomposite. (**A**) Fourier transformed infrared transmittance spectra of AgNW and LE-AgNW. Black and red lines represent peak absorption spectra of AgNW and LE-AgNW, respectively. (**B**) The electrical conductivity of LE-AgNW/SBS nanocomposite as a function of LE-AgNW concentration ($n \geq 3$). (**C**) The Young's modulus of LE-AgNW/SBS nanocomposite as a function of LE-AgNW concentration ($n \geq 3$).

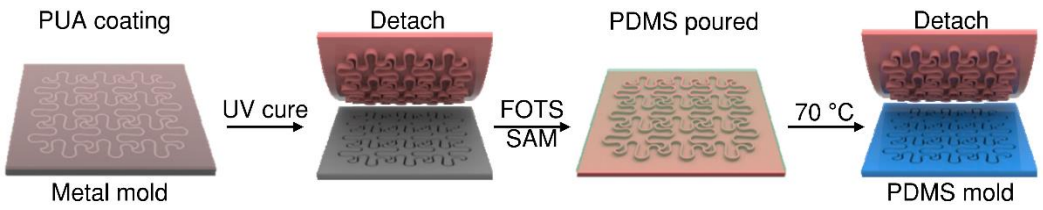

Fig. S2. PDMS mold fabrication process for the epicardial mesh. Schematic illustrating the fabrication of a serpentine-shaped PDMS mold from a metal template. The replicated PDMS mold was used to create the LE-AgNW/SBS mesh with the serpentine pattern. PUA, polyurethane acrylate; UV, ultraviolet; SAM, self-assembled monolayer; FOTS, trichloro(1H,1H,2H,2H perfluorooctyl)silane.

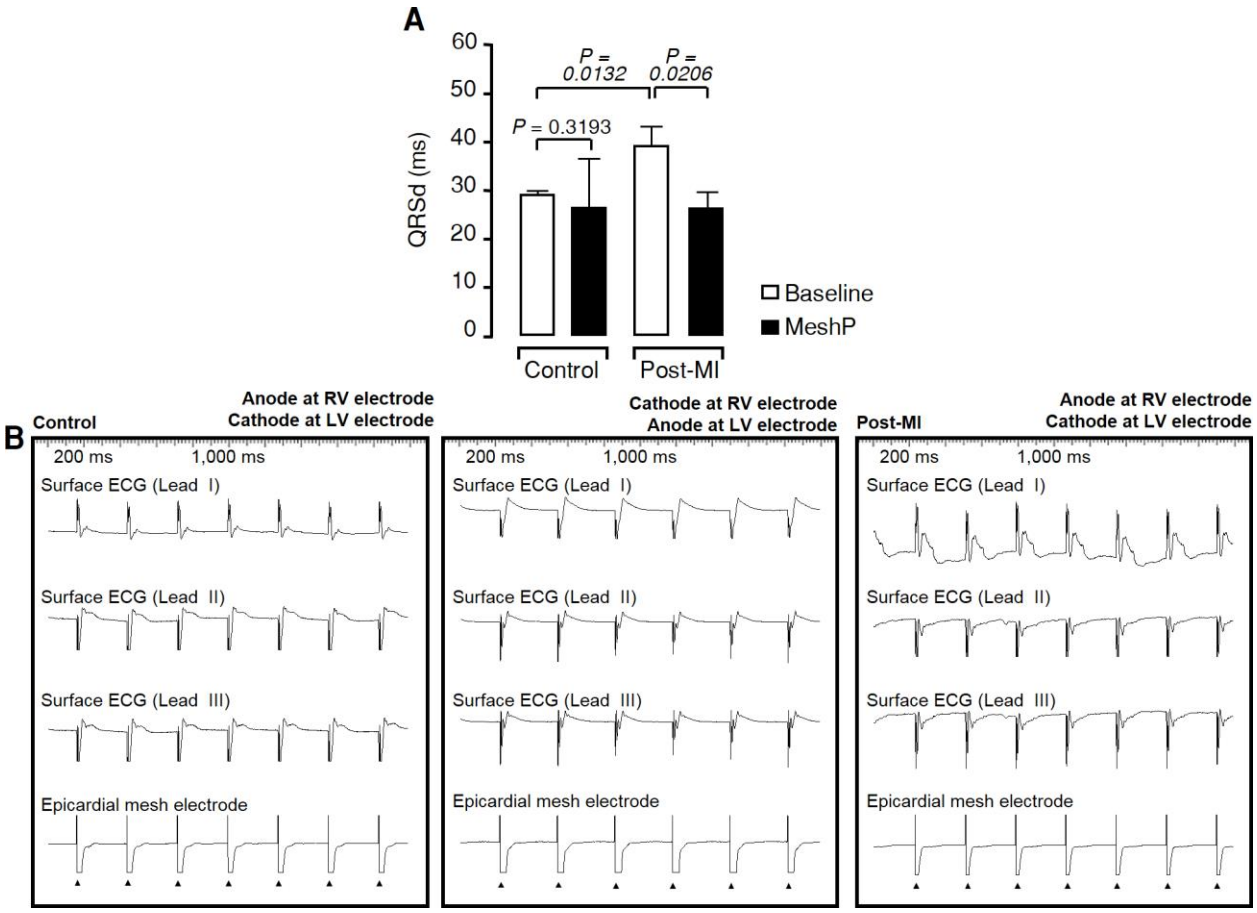

Fig. S3. Electrical stimulation by the epicardial mesh. (**A**) The effect of electrical stimulation by the epicardial mesh on QRS durations in control (n = 9) and 8-week post-infarct (Post-MI) rats (n = 12). Epicardial mesh pacing (MeshP) was performed in 8 of the 9 controls (one died during procedure). MeshP was accomplished in 10 of the 12 post-MI rats (two died during procedure). The cycle length of MeshP was 280 ms. P values determined by unpaired Student's t-test. (**B**) Surface electrocardiogram strips (leads I, II, and III) were recorded during electrical stimulation by the epicardial mesh in representative control and post-MI rats (left and right panel). Middle panel shows electrograms during electrical stimulation after changing polarity of the mesh electrodes in a control rat. QRS durations are not different between those. The average pacing threshold of the epicardial mesh was 1.1 ± 0.2 mA (SEM).

A

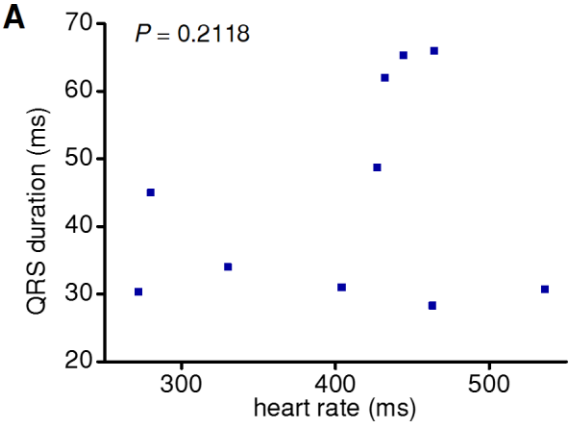

B

No	Baseline		Mesh pacing at cycle lengths of 280ms	
	heart rate (ms)	QRS duration (ms)	Percentage pacing cycle lengths	QRS duration (ms)
Post-MI Rat #1.	280	45	90%	26
Post-MI Rat #2.	272	30.3	90%	21

Fig. S4. The relation of heart rates to QRS durations, and epicardial mesh pacing at 90% of the baseline cycle lengths. (**A**) The correlation of heart rates and QRS duration at baseline. Data are individual post-MI rats (n = 10). P value determined by the Pearson correlation test. (**B**) The effect of pacing at 90% of baseline cycle lengths on QRS duration. Data are for n = 2 post-MI animals from (A), before and after pacing at 90%. The animals were chosen because their baseline heart rates were similar to the pacing rates.

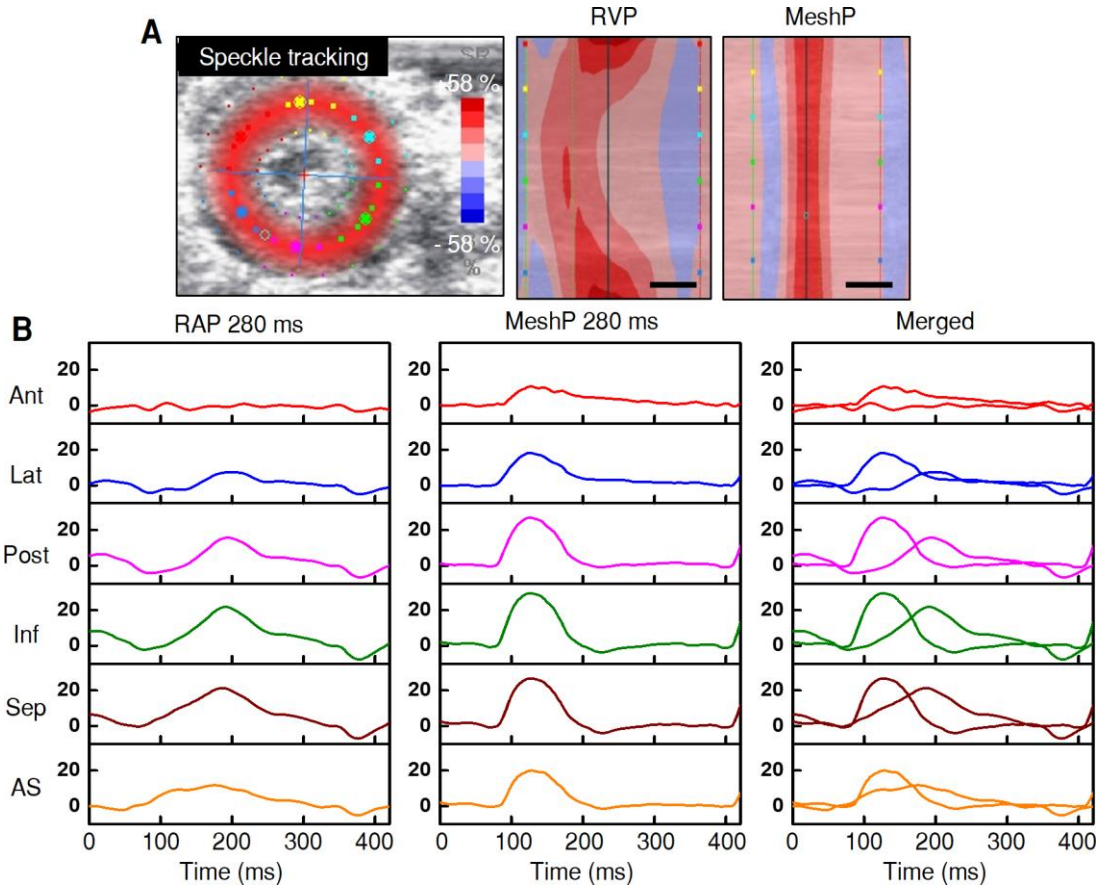

Fig. S5. Speckle tracking radial strain. (**A**) A speckle tracking strain image to demonstrate methodology. The curves are color coded by the defined myocardial regions as depicted in the middle and left panel. The left panel indicates the color-coded 2D mode at baseline (sinus rhythm), reflecting synchronous contraction at systole. The color-coded M-mode in the middle panel demonstrates dyssynchronous contraction during right ventricular pacing (RVP) which represents a positive control. In contrast, synchronous contraction can be seen after electrical stimulation by the epicardial mesh (MeshP; right panel). Scale bars, 100 ms. (**B**) Dyssynchronous myocardial contraction in an 8-week post-myocardial infarction (MI) heart and recovery to synchronous activity by MeshP. Right atrial pacing (RAP) shows dyssynchrous contraction; standard deviation of time to peak systolic strain (black dash) in all 6 segments was 33 ms. In contrast, electrical stimulation with the MeshP shows synchronous activation of all segments; standard deviation of time to peak systolic strain in all 6 segments was 1 ms.

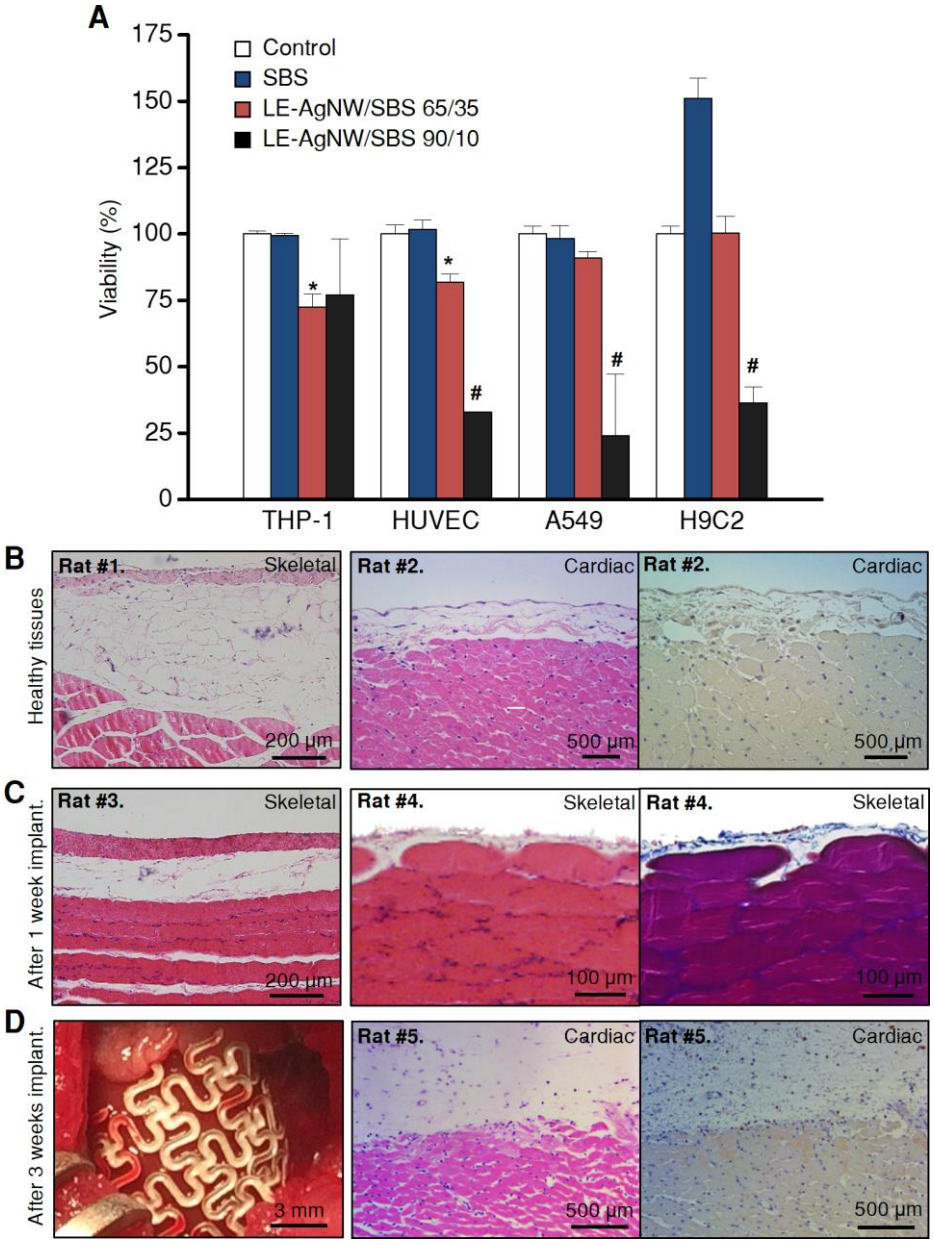

Fig. S6. Evaluation of cytotoxicity of the LE-AgNW/SBS film. (**A**) Cell viability assays of control, SBS film, LE-AgNW/SBS film (65:35 ratio), and LE-AgNW/SBS film (90:10 ratio) in THP-1, HUVEC, A549, and H9C2 cells in vitro. Cells were exposed to materials for 12 h at 70% confluence. $^{*}P < 0.05$, $^{\#}P < 0.0001$ versus control, unpaired Student's *t*-test. Data are means ± SEM ($n = 4$). (**B**) Representative H&E stains (left and middle panels) and macrophage assay (F4/80, right) from healthy rodent skeletal and cardiac tissues without epicardial mesh implantation. (**C**) Epicardial meshes composed of LE-AgNW/SBS (65:35) implanted in the skeletal muscle for one week. Representative H&E stain (left and middle panels) and Masson's trichrome histology (right panel). (**D**) H&E stain (middle panel) and macrophage assay (F4/80, right) from one rat heart (left) where an epicardial mesh was implanted for 3 weeks.

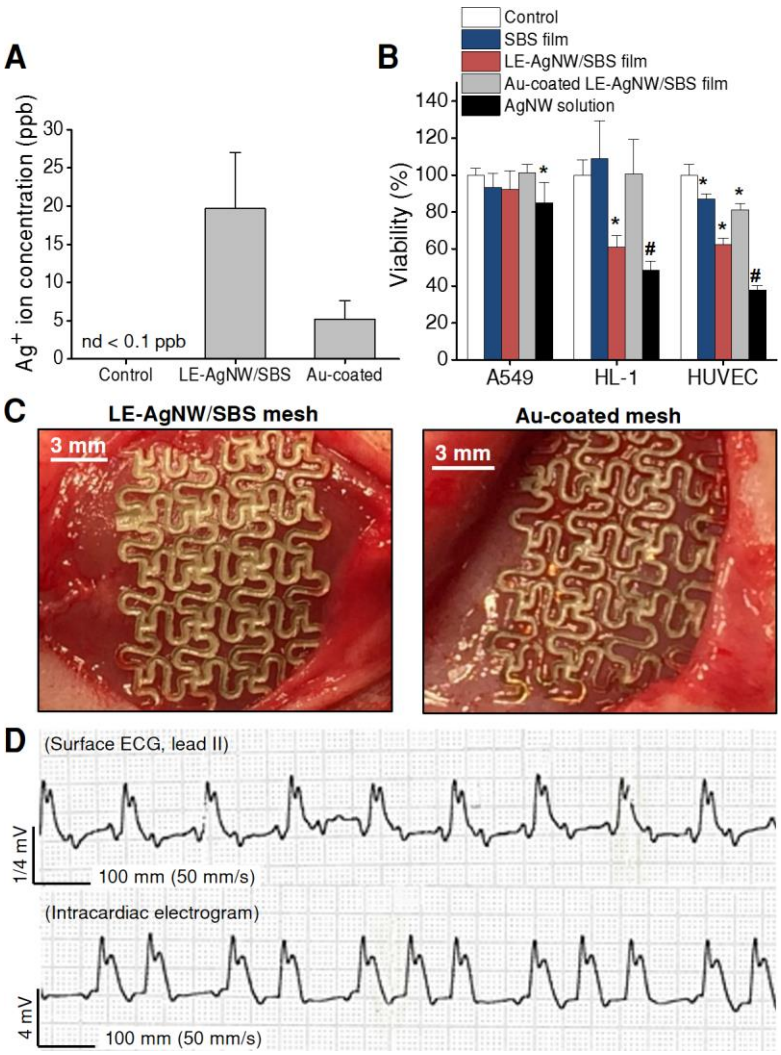

Fig. S7. Feasibility and safety test of the gold-coated epicardial mesh. (**A**) ICP-MS analysis of the epicardial mesh (LE-AgNW/SBS) and Au-coated epicardial mesh after 10 days in PBS solution. Data are means ± SEM (n = 3). (**B**) Evaluation of cytotoxicity of Au-coated LE-AgNW/SBS film, LE-AgNW/SBS film, and AgNW. Cells were exposed to materials at a 70% confluence. Viability tests were performed in A549, HL-1, and HUVEC cells for 24 h after seeding. $^{*}P < 0.05$, $^{\#}P < 0.0001$ versus control, unpaired Student's t-test. Data are means ± SEM (n = 4). (**C**) Photographs of the LE-AgNW/SBS mesh and Au-coated LE-AgNW/SBS mesh implanted in femoral muscles. (**D**) Representative surface electrocardiogram (ECG, lead II, top trace) and intracardiac electrogram recorded from the Au-coated epicardial mesh encircling the rat heart (bottom trace).

Table S1. Echocardiographic data in control and 8-week post-MI rats. MeshP, epicardial mesh pacing; LVEDD, left ventricular end-diastolic dimension; LVESD, left ventricular end-systolic dimension; FS, percentage fractional shortening.

Group	Rat #.	Baseline			MeshP		
		LVEDD (mm)	LVESD (mm)	FS (%)	LVEDD (mm)	LVESD (mm)	FS (%)
Control	1	0.7	0.33	52.86	0.54	0.26	51.85
	2	0.53	0.25	52.83	0.52	0.21	59.62
	3	0.52	0.26	50.00	0.54	0.24	55.56
	4	0.68	0.32	52.94	0.5	0.21	58.00
Post-MI	5	0.47	0.39	17.02	0.44	0.32	27.27
	6	0.48	0.37	22.92	0.4	0.27	32.50
	7	0.62	0.48	22.58	0.44	0.3	31.82
	8	0.88	0.66	25.00	0.77	0.54	29.87
	9	0.6	0.45	25.00	0.45	0.27	40.00

Table S2. Speckle tracking radial strain data in control and 8-week post-MI hearts. AS, anteroseptal; Ant, anterior; Lat, laterial; Post, posterior; Inf, inferior; Sep, septal.

Group	Rat #	Baseline					
		AS (%)	Ant (%)	Lat (%)	Post (%)	Inf (%)	Sep (%)
Control	1	42.65	45.7	52.6	44.08	47.12	50.33
	2	31.95	32.97	33.57	30.4	29.27	31.92
	3	28.59	28.2	26.35	27.81	26.34	25.05
	4	43.05	47.57	54.75	42.22	44.74	50.91
	5	30.79	32.78	35.55	30.44	31.57	34.15
Post-MI	6	7.69	6.41	8.37	7.46	8.77	10.12
	7	15.31	15.36	16.4	15.82	16.53	17.31
	8	9.54	8.22	5.77	12.55	12.75	6.98
	9	15.21	10.54	2.19	12.33	5.81	1.42
	10	20.4	16.96	15.77	16.78	18.99	21.45
	11	14.51	13.03	8.68	13.32	9.85	6.01
Group	**Rat #**	**MeshP**					
		AS (%)	Ant (%)	Lat (%)	Post (%)	Inf (%)	Sep (%)
Control	1	35.87	32.1	34.2	39.08	38.5	38.21
	2	28.19	28.41	30	30.66	34.61	37.12
	3	28.3	30.32	34.13	28.99	32.83	37.87
	4	34.23	32.93	32.37	36.05	37.17	34.36
	5	64.67	64	43.84	52.68	43.26	39.83
Post-MI	6	12.22	12.5	17.96	15.81	22.42	28.07
	7	23.8	26.26	28	22.4	22.62	24.88
	8	12.99	12.87	14.2	13.81	14.74	15.58
	9	21.55	21.01	14.3	16.21	8.3	7.12
	10*	-	-	-	-	-	-
	11	27.23	33.5	38.98	22.95	22.91	30.75

*The #10 post-MI rat died due to arrhythmic event prior to epicardial mesh pacing (MeshP).

Table S3. LV contractility index, dP/dt_{max}, in controls and 8-week post-MI rats. RAP, right atrial pacing; MeshP, epicardial mesh pacing.

Group	Rat #	dP/dt_{max} (mmHg/ms)	
		RAP	MeshP
Control	1	3840	3355
	2	3159	5631
	3	3503	2795
	4	4838	6179
	5	1902	1057
Post-MI	6	1386	1667
	7	3087	2949
	8	1542	2031
	9	3523	4016
	10	2278	2783